Compressible pairwise interaction extended point-particle model for force prediction of shock-particle bed interaction

Smyther S. Hsiao, Kambiz Salari, and S. Balachandar

Phys. Rev. Fluids **8**, 054301 — Published 30 May 2023

DOI: 10.1103/PhysRevFluids.8.054301

Compressible Pairwise Interaction Extended Point-Particle Model for Force Prediction of Shock-Particle Bed Interaction

Smyther S. Hsiao
Department of Mechanical & Aerospace Engineering,
University of Florida, Gainesville, FL, 32611-6250

Kambiz Salari
Lawrence Livermore National Laboratory, Livermore, CA, 94550

S. Balachandar*
Department of Mechanical & Aerospace Engineering,
University of Florida, Gainesville, FL, 32611-6250

(Dated: May 12, 2023)

We propose a pairwise influence framework for the complex unsteady compressible particle-laden flow problem by accounting for the scattered hydrodynamic waves emitting from neighboring particles in an Euler-Lagrange simulation. It has been observed from particle-resolved (PR) simulations of randomly dispersed particle beds under a loading shock that the compressible pseudo-turbulence dominates the flow system even after the primary shock has passed, which causes fluctuations observed in the forces experienced by the particle. Moreover, the fact that each particle exists in the vicinity of a random arrangement of other particles modifies the time history of the drag force experienced by each particle during and after the passage of the shock. First, the scattering flow field due to an incoming shock interacting with a single sphere is constructed using an analysis of the flow in the acoustic limit. Then we examine the validity of the compressible Maxey-Riley-Gatignol force model by comparing the force prediction against a PR simulation of two interacting particles for various particle arrangements and incoming shock strength. Subsequently, the neighboring influences are stored as a library of maps that can be used readily in the calculation of the perturbation force. Finally, the pairwise interaction assumption is evaluated by comparing the force predicted with the model with PR simulations of a randomly packed particle bed of 10% volume fraction for both water and air as the fluid medium for an incoming shock Mach number 1.22. With a considerably lower cost for the implementation of the model compared to PR simulations, it is verified that the model is reasonably accurate in pinpointing particles whose peak force is significantly larger or smaller than the mean drag but also to capture the prolonged fluctuations after the initial shock.

I. INTRODUCTION

Numerical and experimental work on the interaction between a planar shock wave and a random distribution of particles (see [14, 29–31, 37, 38, 41, 42, 46]) highlights the rich flow phenomena in such systems. The force on the particles remains zero before the shock arrival, rapidly increases to a maximum when the shock is located approximately near the particle center, then slowly decays to a value that corresponds to the post-shock uniform flow. Although the above general trend is followed by all particles, the actual force history experienced by each particle within the random distribution substantially differs from one to another. In particular, particle-to-particle variation of key quantities, such as the magnitude of peak force, the time at which the peak force is realized, and the steady force long after the passage of the shock, is comparable in magnitude to their mean values averaged over the entire bed of particles. This particle-to-particle variation in force experienced by the different particles is due to interaction among the randomly distributed particles [9, 38].

All the particles within the bed see nominally the same shock propagating past them. However, as the moving shock touches the first layer of particles, the incident primary shock wave is both transmitted through the particle layer and reflected backward. Upstream particles interacting with the incoming shock produce disturbances that travel with the incoming shock downstream to other particles, thus creating a different local flow condition for the downstream particles. Additional disturbances from the downstream particles travel upstream and can exist in between particle pairs. Interaction between the transmitted waves can create shock focusing effect, but in general, the total energy dissipates as the first shock penetrates deeper into the bed [37, 38]. Thus, in addition to the primary shock, each

---

* bala1s@ufl.edu

particle also sees the waves emanating from all other particles that are located upstream and downstream. The perturbation flow due to the neighboring particles has a substantial influence in altering the force experienced by each particle.

From the perspective of the fluid flow, the compressible flow passing through the bed of particles substantially differs from the standard uniform post-shock flow behind a propagating planar shock. A substantial amount of spatial and temporal fluctuation is generated around the particles contributing to the chaotic nature of the flow within the bed and these fluctuations are termed *pseudo turbulence*. The complex particle-to-particle variation seen in the force evolution of each particle is due to the perturbation flow or pseudo turbulence generated by its neighbors [34, 45, 55]. Several mechanisms, including flow acceleration due to the blockage effect of the particles, transmitted waves around the particles, and waves that are reflected off the particles, contribute to pseudo turbulence.

The interaction between different particles in the cluster is extremely complicated. Even in the case of a steady high-speed compressible flow over a random distribution of particles, each particle is subjected to the near wake, far wake, and the recompression region created by other particles in the neighborhood [11, 41, 42, 51, 56]. Experimental works that analyze the motion of multi-spheres are also insightful but such analysis is hard to achieve due to the rapid evolution of the particles. Park and Park [43] conducted experiments in a shock tunnel with free-stream Mach number 6 and performed separation trajectory analysis for single and multiple spheres aligned in a ring shape. Whalen and Laurence [56] designed a suspension gadget that enabled the release of numerous equal-sized spheres.

Other works have addressed the force estimation on a sphere under the influence of a disturbing neighbor in the compressible flow regime. Laurence et al. [27] based their estimation on the analytical blast wave analogy in both two and three-dimensions in the hypersonic regime. One of the interesting phenomena observed in their study, dubbed shock-wave surfing, is also studied extensively in Laurence and Deiterding [26]. Marwege et al.[32] provided an insightful means to estimate forces experienced by bodies immersed in the compressible wake of a leading sphere under steady compressible incoming flow. Register et al. [47] also studied the trajectory of a second particle by time-marching it with the aid of a finely-computed force map, which was constructed using steady-state two-sphere simulations.

A. Pairwise Modeling Approach

The pairwise interaction extended point particle (PIEP) approach has proven to be successful in explaining the complex interaction between the flow and a random distribution of particles in the incompressible steady flow limit [2, 39]. The overarching goal is to develop a similar theoretical framework that can explain shock interaction with a distribution of particles.

Particle-resolved (PR) simulations of particle-laden compressible flows offer direct access to all the above-mentioned complex flow physics. However, PR simulations of shock-particle interaction pose a great computational challenge. The wide range of lengths and time scales in the system increase the simulation cost and thus hinder the simulation of a large distribution of particles. When compared to the size of the particle, one typically needs $O(10^4)$ grid points resolving the particle surface in order to capture the diffraction of the shock waves and the post-shock flow around the particle [37]. As a result, PR simulations of shock-particle interaction have typically been limited to systems consisting of hundred to thousand of particles [9, 35, 38]. For practical applications consisting of millions of particles, one must resort to Euler-Lagrange (EL) or Euler-Euler (EE) approaches [5, 10, 12, 13, 52–54, 58].

In the EL approach, the fluid phase is treated in the Eulerian frame, while particles are individually tracked or followed in the Lagrangian frame of reference. Furthermore, the grid resolution is typically chosen to resolve the large-scale features of the flow and therefore will be of the order of a particle diameter or larger. Since the flow is not resolved on the scale of a particle, a first-principle evaluation of force on the particle is not possible. A point-particle model must be employed, which models the instantaneous force on the particle as a function of the state of the flow surrounding the particle. For accurate prediction of the force, the state of the surrounding flow must be properly characterized by taking into account both the macroscale flow (i.e., the planar shock and the post-shock flow) and the pseudo turbulence generated by the neighboring particles. This leads to the following three fundamental challenges to accurate point-particle modeling of shock interaction with a random distribution of particles: (i) Compressible flow features such as shocks and contact discontinuities are often much thinner than the particle diameter. Therefore, even the macroscale flow around the particle cannot be taken to be spatially uniform on the scale of the particle. (ii) The time scale of shock crossing a micron-sized particle is of the order of only nanoseconds. Thus, the particle sees a highly-transient flow as the shock passes over it, and the unsteady effect must be properly accounted for in the point-particle model. (iii) As discussed earlier, each particle also sees the pseudo turbulence generated by its neighbors which must also be accounted for in the point-particle model if we want to capture the substantial particle-to-particle variation in shock-induced force.

Commonly used point-particle models, such as the standard drag model, do not account for the above challenges. To capture the effect of rapid time variation one must adopt the Basset–Boussinesq–Oseen (BBO) equation to calculate the unsteady force on the particles [15]. In the present context of shock interaction with a random distribution of particles, the compressible version of the BBO equation (C-BBO) must be used [4, 44]. It must be noted that the unsteady force on a particle depends on the history of flow as the shock passes over the particle. Spatial variation of the surrounding flow on the scale of the particle requires the use of the compressible Maxey–Riley–Gatignol (C-MRG) equation [4, 16, 33, 44] in the particle force calculation. The C-MRG equation is qualitatively similar to the C-BBO equation, except that the undisturbed fluid properties are expressed as surface and volume averages over the particle.

The accuracy of the C-MRG equation for predicting the force on an isolated particle with air and water as the ambient fluid medium has been established [8]. The performance of the C-MRG model was substantially better and highlighted the importance of the unsteady and nonuniform nature of the planar shock propagating over a particle. It must be emphasized that all point-particle models, including the C-MRG model, are based on the undisturbed flow seen by the particle, where undisturbed flow refers to the flow that would exist in the absence of the particle. In the case of an isolated particle, the undisturbed flow is simply the planar shock propagating over the particle. In the case of a planar shock propagating over the distribution of particles, the undisturbed flow of a particle includes the pseudo turbulence created by all other neighbors. Since the details of pseudo turbulence are not known in an EL or EE simulation, the undisturbed flow of a particle within a random distribution must be approximated. It is noted that the C-MRG model, like other point-particle models, requires the undisturbed flow of the particle to be not corrupted by the self-induced velocity of the particle. If the self-induced perturbation is substantial, then a correction procedure is required to extract the true undisturbed flow of the particle. Such correction procedure has been developed in the incompressible regime [6, 7, 17, 22, 24], but not in the compressible regime. The self-induced perturbation will not be an issue in the present work.

We now address the challenge of calculating the undisturbed flow of a particle (henceforth referred to as the *reference particle* whose time evolution of force is the quantity of interest) taking into account the pseudo turbulence created by its neighbors. In an EL simulation, pseudo turbulence is a sub-grid quantity that is not computed and therefore must be modeled. Pseudo turbulence and its effect must be evaluated based on the following macroscale information: the planar shock flow approaching the particle (i.e., the macroscale flow) and the microscale information of the relative location of the neighboring particles. In the context of steady incompressible flow over a random distribution of particles, Akiki et al. [2, 3, 39] introduced the concept of pairwise interaction extended point-particle (PIEP) model where pseudo turbulence was modeled as a superposition of perturbation flow generated by each neighbor in response to the ambient flow around it. They observed that the application of the MRG model (because of the incompressible flow) using the pairwise superposition of the perturbation flows of neighbors yielded a good prediction of the particle-to-particle variation in the force.

The primary purpose of this paper is to develop a compressible pairwise interaction extended point-particle (C-PIEP) framework and test its ability to predict the force on a particle in the presence of neighbors subjected to a propagating planar shock. The compressible nature of the present problem adds to the complexity of modeling pairwise interaction [2, 3, 48, 49]. More specifically, the problem of shock-particle interaction is inherently unsteady, while previous development of pairwise interaction perturbation flow and force maps have been in the context of steady flows. Extension of these maps to unsteady conditions and proper accounting of the unsteady forces within the framework of pairwise superposition is not straightforward.

We simplify the modeling task by considering the small time limit. We will consider the short-time pairwise superposition of force on a particle immediately following the propagation of a shock. The time-dependent nature of the perturbation flow will be accounted for with an analytic solution that is available in the acoustic limit. The compressible unsteady force map will be developed under the linear assumption of inviscid weakly-compressible perturbation. This allows the use of a classical acoustic scattering solution. The setup consists of a pair of *disturbing-disturbed spheres* that are subjected to an incoming weak planar shock. We are interested in analytically calculating the perturbation flow generated by the *disturbing sphere* and its influence on the force history of the *disturbed sphere*. This setting is analyzed with a fundamental solution of the acoustic field (see Hasegawa and Yosioka [18], Lamb [21], and Morse [40]).

As a planar shock propagates over a pair of particles, the force on the reference perturbed particle is calculated with the C-MRG model with the undisturbed flow over the reference disturbed particle approximated as a superposition of the undisturbed planar shock wave and the perturbation flow computed with the acoustic scattering solution of a shock wave around the perturbing neighboring particle. The results of the C-MRG model are compared against those obtained from corresponding two-particle PR simulations. The C-MRG model will allow for the investigation of contributions arising from pressure-gradient and inviscid unsteady force components. The contribution to the two force components from a perturbing neighbor is stored as respective perturbation maps. Using these maps, the perturbing influence of each neighbor can be evaluated and added to obtain the total perturbation force. The utility of this pairwise superposition approach will be evaluated by comparing its prediction against corresponding PR simulation results.

This paper is organized as follows: In Section II, as the first step of pairwise interaction model development, we start with a closed-form solution of acoustic scattering solution of a weak shock by a sphere. The acoustic approximation is then validated against particle-resolved simulation results. In Section III we then present the compressible Maxey-Riley-Gatignol (C-MRG) force model and its validation against PR simulation results at the level of two interacting particles. Then in Section IV, the approach is extended to a random array of particles using the compressible pairwise interaction approximation and demonstrated against PR-simulation results of shock propagation over a random distribution of particles. This section also presents the force component maps obtained from the acoustic limit solution. Finally, conclusions are drawn in Section V.

II. UNSTEADY COMPRESSIBLE PIEP MODEL

A. Closed-Form Solution of Scattering of a Weak Shock by a Sphere

The aerodynamic force on the disturbed reference sphere will be evaluated in terms of its undisturbed flow using the C-MRG model. In this section we start with the compressible Navier-Stokes equations and obtain an explicit expression for the undisturbed flow of the reference particle subjected to a weak shock in the presence of another disturbing sphere:

$$\frac{\partial \rho}{\partial t} + \nabla \cdot (\rho \boldsymbol{u}) = 0 \tag{1}$$

$$\frac{\partial (\rho \boldsymbol{u})}{\partial t} + \nabla \cdot (\rho \boldsymbol{u}\boldsymbol{u}) = \nabla \cdot \sigma \,, \tag{2}$$

where ρ is the density of the fluid, $\boldsymbol{u}$ is the fluid velocity, and σ is the stress tensor, which for an inviscid flow reduces to $-p\boldsymbol{I}$. The flow is assumed to be isentropic, so pressure p is a function of fluid density. The undisturbed flow of a particle will include both the original planar shock, which corresponds to the macroscale component, and the scattered flow field of the disturbing neighbors, which corresponds to the microscale component of the undisturbed flow.

We consider a planar shock approaching two nearby spherical particles, one of which is the disturbed or the reference particle, the modeling of whose force is the object of interest, while the other is the disturbing particle. The incoming planar shock is denoted by the superscript ^{in} and the perturbation flow due to the scattering by the disturbing neighbor is denoted by the superscript ^{sc}. Thus, the pressure, density, and velocity fields that the reference particle is subjected to can be represented as

$$p^{un} = p_0 + p^{in} + p^{sc}, \quad \rho^{un} = \rho_0 + \rho^{in} + \rho^{sc}, \quad \boldsymbol{u}^{un} = \boldsymbol{u}^{in} + \boldsymbol{u}^{sc} \tag{3}$$

where ρ_0 and p_0 are respectively the background density and pressure, while the background velocity is zero. The superposition gives the *undisturbed flow* of the reference particle and is denoted by the superscript ^{un}.

Substituting (3) into (1) and (2) and linearizing we obtain the following equations for the scattering part

$$\frac{\partial \rho^{sc}}{\partial t} + \nabla \cdot (\rho_0 \boldsymbol{u}^{sc}) \approx 0 \,, \quad \text{(4a)} \qquad \frac{\partial (\rho_0 \boldsymbol{u}^{sc})}{\partial t} \approx \nabla \cdot (-p^{sc}\boldsymbol{I}) \,, \quad \text{(4b)} \qquad \text{and } p^{sc} \approx c_g^2 \rho^{sc} \,, \quad \text{(4c)}$$

where c_g is the post-shock speed of sound.

The incoming and scattered velocity fields can be written in terms of velocity potentials as $\boldsymbol{u}^{in} = \boldsymbol{\nabla}\phi^{in}$ and $\boldsymbol{u}^{sc} = \boldsymbol{\nabla}\phi^{sc}$. If we consider a monochromatic incoming plane wave of a unit amplitude of the form $\boldsymbol{u}^{in} = exp\{-i(kz - \omega t)\}\boldsymbol{e}_z$, the corresponding incoming velocity potential can be expressed as [4]

$$\phi^{in} = \sum_{n=0}^{\infty} C_n (2n+1)(-i)^n j_n(kr) P_n(cos\varphi) e^{i\omega t} \,, \tag{5}$$

where j_n is the spherical Bessel function of the first kind of order n, P_n is the Legendre polynomial of the first kind of order n, and $C_n = i/k$ is the amplitude (note $i = \sqrt{-1}$). The wavenumber k and frequency ω are related by $\omega/k = c_0$, where c_0 is the the pre-shocked ambient speed of sound. In this work, a spherical coordinate is used with r being the radial direction, θ defined as the azimuthal angle, and φ as the polar angle. The flow direction z is then defined as $z = r\,cos\varphi$. When the monochromatic wave is scattered by the disturbing sphere, the scattered potential can be expressed as

$$\phi^{sc} = \sum_{n=0}^{\infty} C_n (2n+1)(-i)^n S_n h_n^{(2)}(kr) P_n(cos\varphi) e^{i\omega t} \,, \tag{6}$$

Using the no-penetration boundary condition on the surface of the scattering sphere, one can solve for the scattering coefficient S_n to obtain

$$S_n = \frac{-\{nj_n(kR) - (kR)j_{n+1}(kR)\}}{nh_n(kR) - (kR)h_{n+1}(kR)} \,, \tag{7}$$

where R is the radius of the sphere. As can be observed from equations (5) and (6), they are not functions of the azimuthal direction θ and therefore the solution has rotational symmetry with respect to the flow direction.

A planar shock propagating along the z-axis is now expressed as a superposition of monochromatic planar wakes as

$$\boldsymbol{u}_{sh}^{in}(z,t) = u_g\, H(-(z - Z_s(t)))\hat{\boldsymbol{e}}_z = \frac{1}{\sqrt{2\pi}} \int \underbrace{\left[u_g \left(\frac{\delta(k)}{2} - \frac{i}{\sqrt{2\pi}k} e^{ikZ_s(t)}\right)\right]}_{\widetilde{u}_{sh}(k)} e^{-ikz} dk \hat{\boldsymbol{e}}_z \,, \tag{8}$$

where u_g is the post-shock gas velocity, H is the Heaviside function, $Z_s(t)$ is the location of the shock front as a function of time, and $\boldsymbol{e}_z$ is a unit vector along the z-direction. From (5) we note that $e^{-ikz}\boldsymbol{e}_z = \nabla\phi^{in}$. Making this substitution we obtain

$$\boldsymbol{u}_{sh}^{sc}(z,t) = \frac{1}{\sqrt{2\pi}} \int \widetilde{u}_{sh}(k)\, \nabla\phi^{sc} dk \,. \tag{9}$$

The density of the incoming shock and the scattered field by the disturbing sphere can be expressed as,

$$\begin{aligned} \rho_{sh}^{in}(z,t) = \rho_g\, H(-(z - Z_s(t)))\boldsymbol{e}_z \; &= \frac{1}{\sqrt{2\pi}} \int \underbrace{\rho_g \Big[\frac{\delta(k)}{2} - \frac{i}{\sqrt{2\pi}k} e^{ikZ_s(t)}\Big]}_{\widetilde{\rho}_{sh}(k)} e^{-ikz} dk \\ \rho^{sc}(z,t) \; &= \frac{1}{\sqrt{2\pi}} \int \widetilde{\rho}_{sh}(k) \frac{-\nabla^2\phi^{sc}}{ik} dk \,, \end{aligned} \tag{10}$$

where ρ_g is the post-shock density. Scattered pressure can then be obtained from the isentropic relation (4c).

1. Numerical Evaluation

We now briefly address the evaluation of the scattered fields through numerical integration of the expressions given in (9) and (10). These evaluations will be made in non-dimensional variables with D as the length scale and c_0 as the velocity scale. Furthermore, noting that the non-dimensional wavenumber and frequency of each monochromatic wave are the same, these integrals are numerically evaluated over the frequency space. The numerical integration introduces two parameters: ω_{tr}, which is the largest frequency considered in the integration by limiting the integrals to $|\omega| < \omega_{tr}$ and N_ω, which is the number of frequencies included in the numerical integration. Thus, the frequency resolution of integration is $\Delta\omega = \omega_{tr}/N_\omega$. Furthermore, in the representation of the scattered velocity potential, the summation given in (5) and (6) must be limited to a large but finite value of n_{tr}, which is the third numerical parameter.

The proper choice of the three numerical parameters, n_{tr}, ω_{tr}, and N_ω is established through simple experimentation. First, the sensitivity of the summation of the scattered velocity potential is investigated based on the magnitude of the n^{th} term. Since the denominator of the scattering coefficient S_n grows larger as n increases, the terms being summed decay with increasing n. It is observed that if the first 300 terms are included in the summation, the neglected higher-order terms are smaller than 10^{-15} times the largest term of the series. As a result, we choose $n_{tr} = 300$.

The convergence with increasing ω_{tr} is presented in Fig. 1(a), where streamwise velocity normalized by u_g at a point $\boldsymbol{x}_p = (0, 0, 2D)$ is presented as a function of time. Note that the velocity presented is u^{un} which includes both the planar shock and the scattered fields. The time axis has been shifted by t_0, which is the time of arrival of the planar shock at the point $\boldsymbol{x}_p$, and normalized by the time it takes for the shock to cross a particle radius (i.e, normalized by $\tau = D/u_s$, where u_s is shock velocity). The flow and the shock propagation are in the z-direction and the disturbing sphere of unit diameter is located at the origin. Without the scattering effect of the disturbing sphere, the velocity would be a unit-step function. Thus, the deviation from the step function is the scattering effect of the disturbing sphere. From the figure, it can be seen that $\omega_{tr} = 500$ is sufficient and this has been verified at other points within the domain. Figure 1(b) shows the same result on a longer time time for varying n_ω. It is clear from the figure that $N_\omega = 1400$ is adequate and this result has been confirmed at other points within the scattered field. In Fig. 1(b) we also plot particle-resolved inviscid simulation results of normalized streamwise velocity at the point $\boldsymbol{x}_p$

for a planar shock propagating past a single sphere of unit radius. The results of the lower Mach number simulation $M = 1.05$ is in reasonable agreement. There are quantitative differences in the magnitude of the predicted post-shock peak and as a result in the subsequent decay rate. These differences are partly due to the finite Mach number of the particle-resolved simulation and the difficulty in capturing sharp discontinuities with a Fourier expansion. It must be pointed out that in the analytical calculation, the gradient and Laplacian of velocity potential are calculated with second-order finite difference approximation to a relative accuracy of 10^{-8}.

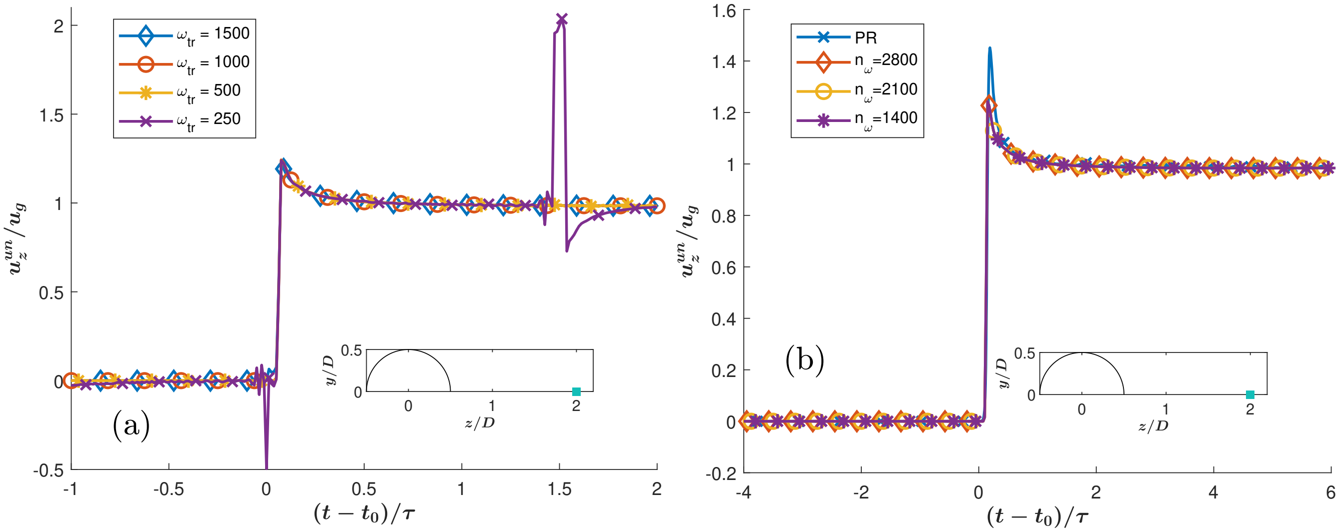

FIG. 1. The plot of normalized streamwise velocity at the point $\boldsymbol{x}_p = (0, 0, 2D)$ analytically calculated with the acoustic scattering theory: (a) Convergence with increasing frequency range included in the integration. Results are shown for $\omega_{tr} = 250$, 500, 1000, and 1500 (n_ω was kept at 1400). (b) Convergence with increasing number of frequency samples used in the integration for $n_\omega = 1400$, 2100, and 2800 (ω_{tr} was kept at 500). Also shown in frame (b) is the particle-resolved simulation result for a shock Mach number of $M = 1.05$.

2. *Arrival Time of the Scattering Signal*

As shown in the schematic presented in Fig. 2, consider the disturbing sphere located at the origin and the disturbed reference sphere located at position $\boldsymbol{x}_r$. We are interested in evaluating the first arrival time of the scattered field from the disturbing sphere to the reference sphere. With the help of the Huygens–Fresnel principle, it is possible to estimate the time it takes for the scattered wave generated at the surface of the scattering particle to travel to the surface of the reference sphere. For the theoretical estimation, we assume the speed of propagation to be at the speed of the shock u_s.

We start by defining the reference time $t = 0$ to be when the planar shock contacts the upstream front of the disturbing sphere. As the shock propagates over the disturbing sphere, the surface point marked A encounters the shock after a time $t_l = l/u_s$, where l is the streamwise distance of point A from the leading edge. Huygens–Fresnel principle states that the point on a wavefront can be viewed as a source for a spherical wavelet. As a result, the scattered field from point A will first arrive at the point marked B on the reference sphere (B lies on the line connecting point A and the center of the reference sphere). The time it takes for an acoustic signal to travel from point A to point B can be evaluated from their distance. Together, the first time of arrival of the scattered field can be evaluated as

$$t_{sc}(z_B, y_B) = \min_{0\le l\le 2} t_{total} = \min_{0\le l\le 2}\left\{\frac{l}{u_s} + \frac{\sqrt{(l-1-z_B)^2 + (y_B - \sqrt{2l-l^2})^2}}{u_s}\right\}, \tag{11}$$

where, without loss of generality, we have assumed the point B to be on the $y-z$-plane and its location $(0, y_B, z_B)$ is a function of l (see Fig. 2). Here the first arrival time is the minimum over all possible values of t_{total}, the total time since the shock first touch the disturbing sphere.

The accuracy of this estimate in the acoustic limit is tested in the following manner. The normalized streamwise velocity of the scattered field only (without the planar shock) evaluated at 10 different points (see inset of Fig. 3(a)) is shown in the figure, where the time axis has been shifted by the estimated first arrival time given in (11) and normalized

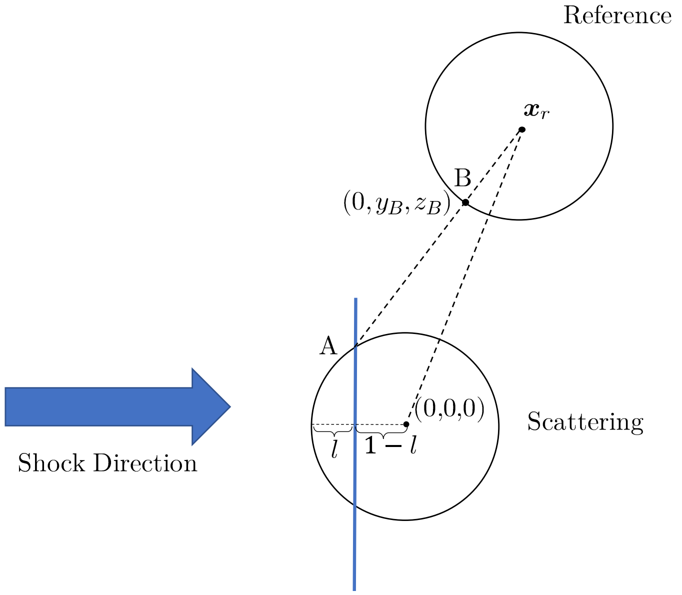

FIG. 2. A schematic illustrating the concept of scattering time t_{sc}, which captures the delay of the signal received by a point B on the reference particle from the instance when the shock (marked as vertical blue line) first touches the scattering sphere. The sphere radius is 1 in this case.

by τ. From the figure, it is clear that the theoretical estimate of first arrival time using the Huygens–Fresnel principle is quite accurate. The corresponding normalized streamwise velocity of the scattered field at the 10 different points computed using a particle-resolved inviscid simulation of a shock propagating over an isolated particle is shown in 3(b).

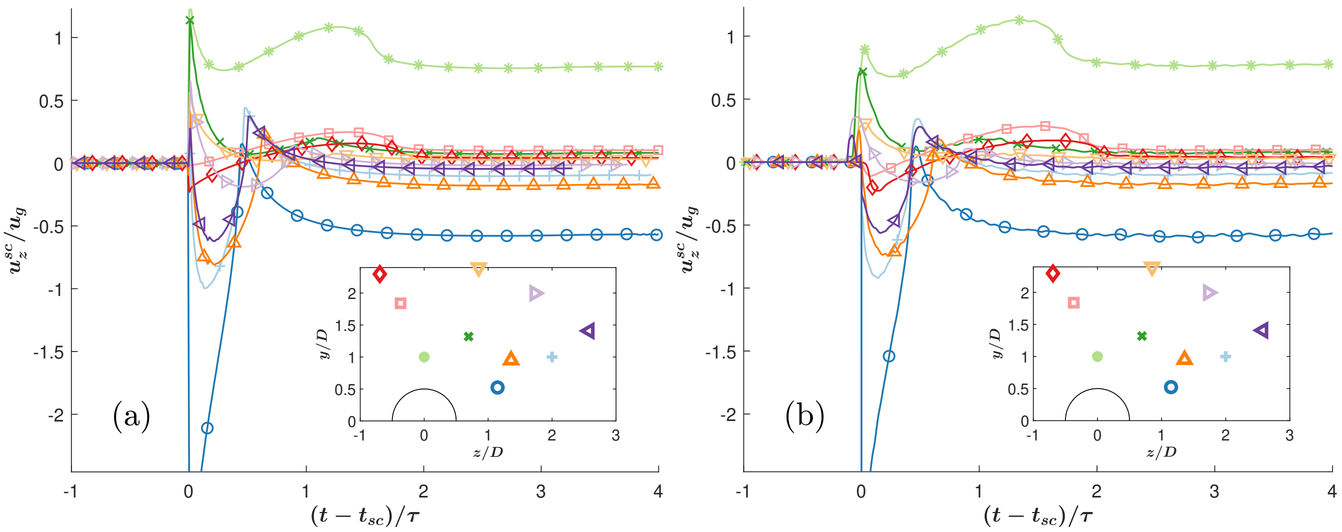

FIG. 3. (a) The velocity signal of the scattered field computed using the acoustic solution (8) at the points shown in the inset. The time axis has been shifted by the first arrival time t_{sc}, which is a function of the location of the individual points. (b) The corresponding scattered velocity plots computed from a particle-resolved simulation at $M_s = 1.05$.

As a further evaluation of the estimation of arrival time, we compute the arrival time at the reference sphere whose center is located at $(0, 3\sqrt{2}, 0)$ and $(0, 3, 0)$ relative to the disturbing sphere, with the shock propagating along the z-direction. The arrival time computed as a function of l for the two different locations is plotted in Fig. 4. In the two cases, the minimum values of $t_{sc} = 1.6803$ and 2.8927 were achieved at $l = 0.39$ and 0.36. These particle locations were chosen since the particle-resolved simulations of Mehta et al. [36] considered these relative locations at a shock Mach number of $M_s = 1.22$. Their observed first arrival times are $t_{sc} = 1.7$ and 2.97 respectively.

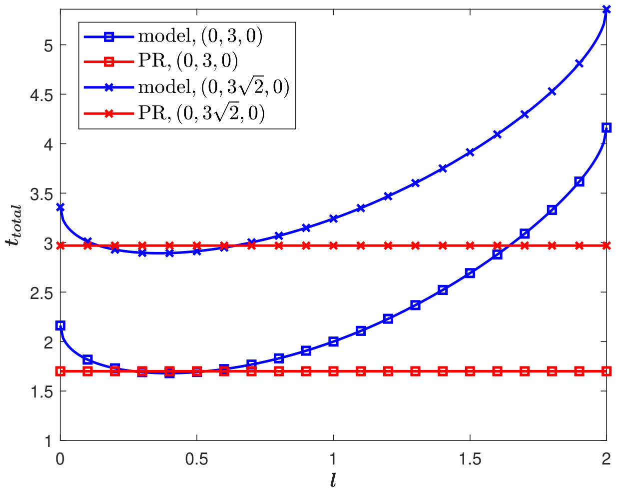

FIG. 4. Time of arrival as a function of l to determine the first time of arrival of the scattered field (blue lines) and the comparison with t_{sc} measured in two-sphere PR simulation (red lines) performed at a shock Mach number of 1.22.

III. PAIRWISE SUPERPOSITION USING C-MRG EQUATION

The C-MRG model of force on a particle due to an undisturbed flow is given by [4, 8, 44]

$$\boldsymbol{F} = \underbrace{-S_p\, \overline{p^{un}\boldsymbol{n}}^s}_{\boldsymbol{F}_{un}} + \underbrace{3\, V_p \int_{-\infty}^{t} K_{iu} \left[\frac{\partial \overline{(\rho \boldsymbol{u}_r)^{un}}^s}{\partial t} + \overline{(\rho \boldsymbol{u})^{un}}^s \cdot \nabla \overline{\boldsymbol{u}_r^{un}}^s \right]_{\xi} d\xi}_{\boldsymbol{F}_{iu}} \; . \tag{12}$$

In the above equation, the first term on the right-hand side, $\boldsymbol{F}_{un}$, corresponds to the undisturbed flow force (also known as the pressure-gradient force) due to the undisturbed flow of the particle. It is simply given by the surface integration of pressure, where $\overline{()}^s$ indicates an average over the surface of the sphere and S_p is the surface area of the sphere (V_p in the second term denotes the volume of the sphere). The surface average is computed with the Lebedev quadrature of order 974 [28], which was found to yield converged values. The second term $\boldsymbol{F}_{iu}$ corresponds to the inviscid unsteady force (which is the compressible analog of the added-mass force) due to the undisturbed flow.

Just as any other force model, the above expression predicts the force on a particle with the undisturbed flow, characterized by the pressure p^{un}, density ρ^{un}, and the velocity fields $\boldsymbol{u}^{un}$ as input. In evaluating the two force contributions given in (12), the undisturbed pressure and velocity are required only on the surface of the particle. Note that in the above expression $\boldsymbol{u}_r^{un}$ is the radial component of undisturbed velocity on the particle surface. The advantage of the above formulation over the standard drag law is that (i) it accounts for the spatial variation of the undisturbed flow on the scale of the particle with the surface and volume averages, and (ii) accounts for the time variation of the undisturbed flow with the history integral in the second term, where K_{iu} is the history kernel and it is a function of the delay time $t - \xi$ and the Mach number based on relative velocity.

The accuracy of the above model has been carefully evaluated in the context of an isolated particle subjected to a planar shock [8]. In this case, since there is no disturbing second sphere as neighbor, the undisturbed flow of the isolated particle is simply given by $p^{un} = p_0 + p^{in}$ and $\boldsymbol{u}^{un} = \boldsymbol{u}^{in}$, where superscript in simply refers to the incident planar shock. Thus, the undisturbed flow of an isolated particle subjected to a shock is known and well-characterized. By comparing the model prediction against particle-resolved simulations for both air and water as the fluid medium, Behrendt et al. [8] established the accuracy of the C-MRG model for the case of an isolated particle.

Our objective here is to use the C-MRG model in evaluating force on a particle where the undisturbed flow includes not only the incident planar shock but also the scattering fields of the neighboring particles. In other words, the undisturbed flow of the reference particle is given by the summation (3). While the macroscale portion of the undisturbed flow is from the incoming shock, the microscale portion due to the scattering of the neighboring spheres will be taken to be the analytical acoustic solution of the previous section. Before we proceed to consider the perturbation flow due to a distribution of neighbors, we will demonstrate the procedure with the disturbance flow created by a single neighbor.

A. Particle-resolved Two-Sphere Simulations

Towards evaluating the accuracy of the C-MRG model in the context of two nearby particles subjected to a planar shock, we have performed particle-resolved inviscid simulations using the in-house finite-volume solver, `RocfluMP`, which solves the governing compressible Euler equations on an unstructured grid. The time evolution of the flow is computed with the fourth-order Runge-Kutta method [19]. Multiple works have confirmed the accuracy of the solver [4, 8, 20, 36, 38]. An example two-particle simulation is shown in Fig. 5 where the two particles are of the same size and are separated 2.5 radii along the flow direction. Thus, as the shock propagates from left to right, the downstream particle is sheltered by the upstream neighbor. The advantage of this inline arrangement is that the flow remains axisymmetric, thus simplifying the computation. The inflow and outflow boundaries are 16 diameters away from the center of the leading sphere. The height of the computational domain is 15 diameters. The spheres are rigid and remain fixed in the domain.

We use 1000 grid points to resolve the surface of each sphere. In the region outside of the sphere, `Triangle` [50], a two-dimensional mesh generator was used to generate 5.9×10^6 elements. The initial condition for the simulation is set up as a shock interface that is placed 0.25 radius upstream of the upstream end of the sphere, as can be seen in Fig. 5. The blue region is the pre-shock gas and the green region is the post-shock gas. Once the simulation starts, the inlet boundary condition (which has the same gas state as the green region) will push the shock downstream and let it interact with the spheres.

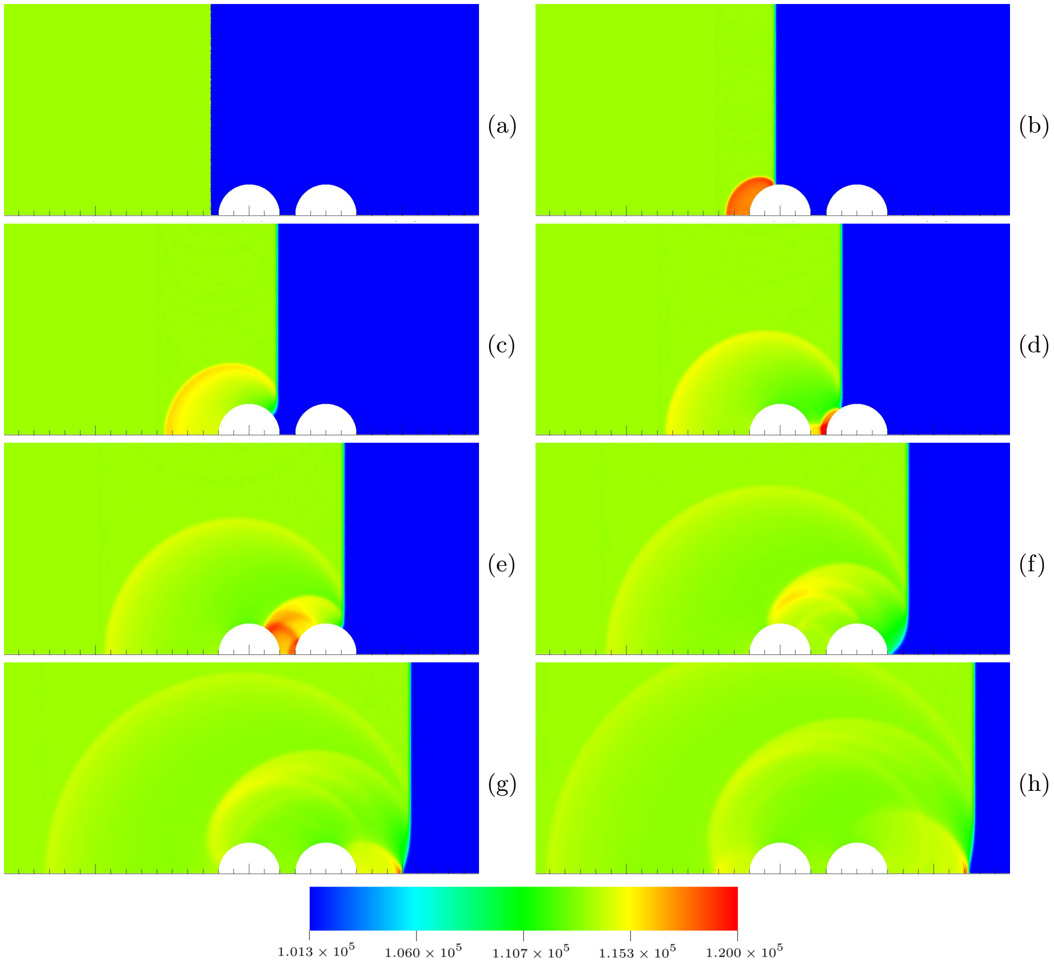

FIG. 5. Snapshots of the two-sphere PR simulation pressure field for an inline arrangement where the centers are separated by a distance of $1.25D$. The spheres are marked in white. Incoming shock Mach number is $M_s = 1.05$. The unit for the colorbar is Pa. The time stamp for each of the figures is (a) 0 s (b) 1.2×10^{-4} s (c) 2.4×10^{-4} s (d) 3.6×10^{-4} s (e) 4.8×10^{-4} s (f) 6×10^{-4} s (g) 7.2×10^{-4} s (h) 8.4×10^{-4} s. Here $\tau = D/u_s = 2.22 \times 10^{-4}$ s.

Figure 5 shows snapshots of the pressure field for a weak shock of Mach number $M = 1.05$. First from Fig. 5(b) one can see that as the shock hits the leading sphere, a stagnation region forms and creates higher pressure in front. Then, as can be seen from Fig. 5(c), the leading sphere blocks part of the incoming shock front and create a delay in shock propagation behind the leading sphere. The shock then hits the front of the second sphere in Fig. 5(d) and creates a higher pressure region. In Fig. 5(e) it is evident that the reflected shock from both the tail of the leading sphere and the front of the trailing sphere bounces back and forth in the region between the two spheres, then propagate outwards in Fig. 5(f). The outward propagating spherical waves keep spreading and lose their strength. As shown in Fig. 5(h), near the centerline, the deformed shock front profile slowly recovers. The time evolution of force experienced by the particles is obtained by surface integration of the computed pressure distributions. Axisymmetric PR simulations were performed for other inline arrangements with different separation distances between the two particles and at other values of shock Mach numbers. The grid resolution of these simulations was comparable and adequate since further refinement did not change the drag force experienced by the reference particle.

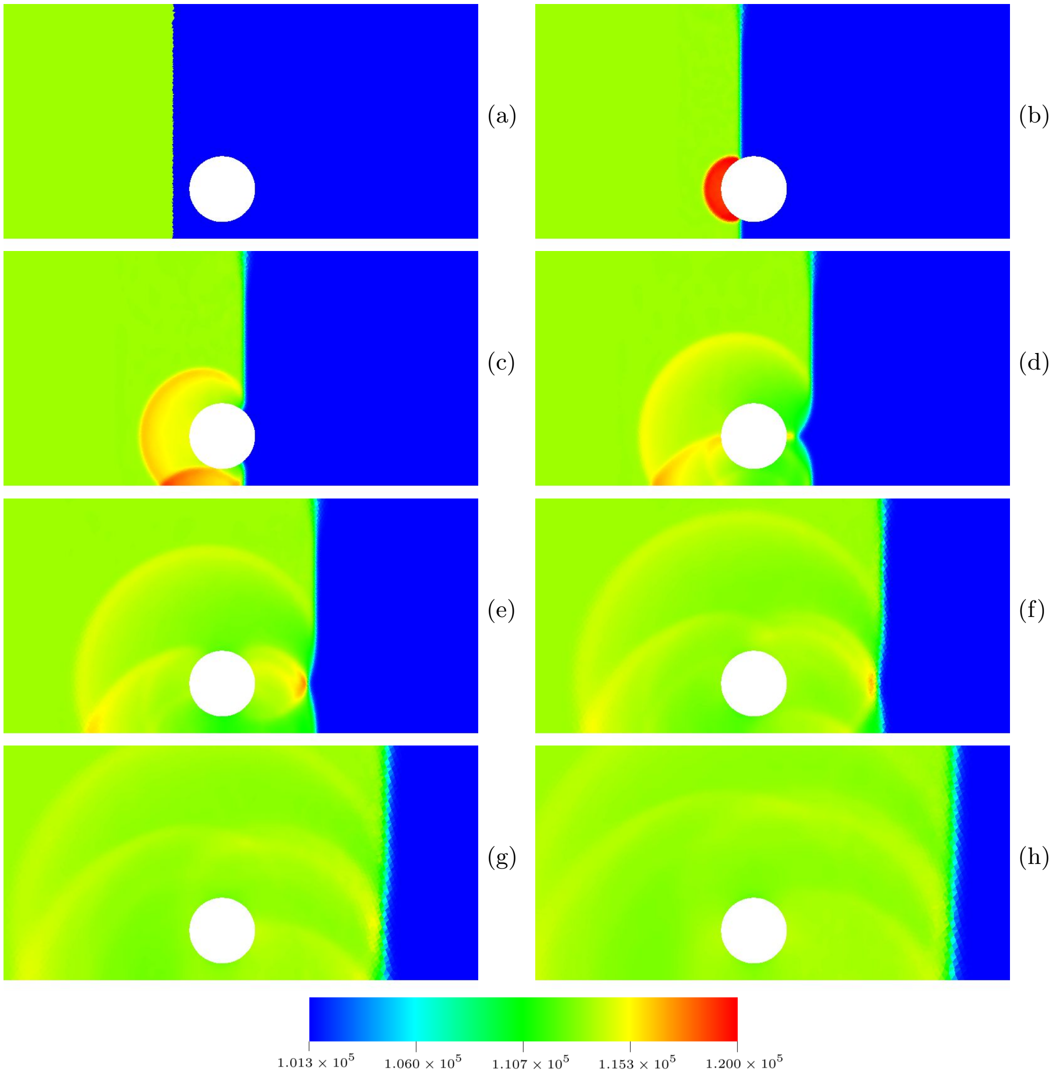

FIG. 6. Snapshots of inviscid PR simulation pressure fields of two side-by-side spheres whose centers are separated by $1.5D$. The spheres are marked in white. Incoming shock mach number is $M_s = 1.05$. The unit for the colorbar is Pa. The time stamp for each of the figures is (a) 0 s (b) 1.2×10^{-4} s (c) 2.4×10^{-4} s (d) 3.6×10^{-4} s (e) 4.8×10^{-4} s (f) 6×10^{-4} s (g) 7.2×10^{-4} s (h) 8.4×10^{-4} s.

PR simulations were also performed for a planar shock propagating over two spheres that are arranged side-by-side with their centers separated by specified distances. The in-line configuration is axisymmetric about the flow direction and thus permits an axisymmetric simulation. The side-by-side arrangement requires a three-dimensional simulation and therefore more expensive. However, the flow is symmetric about both the bisector plane that is normal to the line connecting the two sphere centers and the plane that slices both spheres in half. This allows simulation in only one-fourth of the simulation domain with symmetry conditions on the two planes. The grids are locally refined around the sphere and the smallest element in the refined region is set to be $1/40D$ [37]. These simulations employ a resolution of 9.5 million grid points in the domain.

B. C-MRG prediction and Comparison with PR Simulation Results

This section will compare the force prediction of the C-MRG model against that obtained from the two-particle PR simulations. Three different two-particle configurations are considered and in all cases, the disturbing particle is taken to be located at the origin and the position of the reference sphere whose force is being considered is varied. The three cases to be compared are: (i) the center of the reference sphere is 1.25 diameters downstream of the disturbing sphere; (ii) the center of the reference sphere is 2.5 diameters downstream of the disturbing sphere; and (iii) the center of the reference sphere is 1.5 diameters displaced along the transverse y direction from the center of the disturbing sphere. First, we test the accuracy of the C-MRG model for a weak planar shock of Mach number 1.05.

In the application of the C-MRG model given in (12) to the shock-two-particle interaction problem, we assume the following superposition to hold in the evaluation of force on the reference particle

$$\begin{aligned}
&\overline{p^{un}\boldsymbol{n}}^{s} = \overline{p^{in}\boldsymbol{n}}^{s} + \overline{p^{sc}\boldsymbol{n}}^{s}\,, \qquad && \overline{(\rho\boldsymbol{u})^{un}}^{s} = \overline{(\rho\boldsymbol{u})^{in}}^{s} + \overline{(\rho\boldsymbol{u})^{sc}}^{s}\,,\\
&\overline{(\rho\boldsymbol{u}_r)^{un}}^{s} = \overline{(\rho\boldsymbol{u}_r)^{in}}^{s} + \overline{(\rho\boldsymbol{u}_r)^{sc}}^{s}\,, \qquad && \overline{\boldsymbol{u}_r^{un}}^{s} = \overline{\boldsymbol{u}_r^{in}}^{s} + \overline{\boldsymbol{u}_r^{sc}}^{s}\,.
\end{aligned} \tag{13}$$

The pressure, density, and velocity fields of the incident shock are known from the propagating planar shock relations. The corresponding scattered fields from the disturbing particle are taken to be those given by the analytic acoustic solution. These superpositions when substituted into the C-MRG equation yield the undisturbed and the inviscid unsteady force components. The total force on the reference particle normalized by $\pi\rho_0 D^2 u_{ps}^2/2$ is plotted as a function of normalized time $(t-t_{sc})/(\tau_{ps})$ in the two-particle cases, where u_{ps} is post-shock fluid velocity and $\tau_{ps} = D/c_{ps}$ is the timescale based on the post-shock speed of sound. In each case, the force predicted by the C-MRG model is compared against the companion PR simulation.

1. *Weak shock comparison*

The comparisons are shown in Fig. 7, where frame (a) shows the C-MRG and PR simulation results of an isolated particle, where $\boldsymbol{F}^{in}$ denotes the C-MRG force prediction of an isolated particle due to only the incident shock. Thus, frame (a) establishes the accuracy of the C-MRG model for an isolated particle in the absence of any scattered field. This comparison establishes the baseline that the C-MRG model is quite accurate in capturing the rapid rise of force as the shock propagates over the front half of the particle. The magnitude and the time of peak force are also well captured. Slight differences appear in the decay of the force as the shock moves over the back half of the particle. It can be noted that the inviscid force becomes negative (i.e., temporarily the inviscid force on the sphere points opposite to the flow direction) as the shock is located slightly downstream of the particle. These features and the good predictive capability of the C-MRG model have been previously discussed [4, 8]. Frame (b) shows the force contribution from the scattered field of the disturbing sphere located 1.25 diameters upstream. This contribution is computed as the difference between the total force experienced by the reference particle in the two-sphere case and the total force experienced by the reference particle in the absence of the second particle. The total force on the reference particle is the sum of forces shown in frames (a) and (b). First, it should be noted that the force due to the scattered field is substantial. The initial sharp negative peak and the subsequent positive peak followed by an oscillatory approach to zero seen in the PR simulations are well captured by the C-MRG model. The arrival times of both the shock and the scattered field are important in determining how they superpose. In the present calculation, the shock arrival time is dictated by the shock speed, and the scattering arrival time is computed by the model.

However, there are important differences. The first is, while the trend of the negative peak is captured well, the magnitude of the sharp peak is underpredicted. The negative peak is due to the neighboring particle blocking part of the shock, such that the shock front goes around the particle and arrives at the reference particle later in time. This delay in time is somewhat mispredicted by the model and this is perhaps due to the linear assumption involved both in the evaluation of the scattered field using the acoustic approximation, as well as in the derivation of the C-MRG model. The second difference is in the distinct bump that can be seen in the PR simulation result after the shock has propagated past the reference particle. In frame (b), this bump can be observed at $(t-t_{sc})/\tau_{ps} \approx 1$. This bump arises from the pressure wave that reverberates in the streamwise gap between the two particles. When the pressure is positive it contributes to a higher force and when negative contributes to a lower force magnitude. This mechanism of wave reflections between the two spheres is not captured in the C-MRG model. The C-MRG model accounts only for the perturbation flow generated by the reference particle in response to its undisturbed flow in an unbounded domain. Whereas, in the presence of the neighbor, the perturbation flow gets reflected off the neighbor. A complete accounting of this inter-particle interaction requires the implementation of the method of reflections pursued in Stokes flow, which is beyond the scope of the C-PIEP model.

Figure 7(c) shows the force contribution from the scattered field of the disturbing sphere located farther upstream at 2.5 diameters. Though the separation between the two spheres has increased, the force due to the scattered field remains substantial. The pattern of the initial sharp negative peak and the subsequent positive peak followed by an oscillatory approach to zero can again be observed, and this trend is well captured by the C-MRG model. The negative peak is still underestimated by the C-MRG model due to reasons mentioned above. It can be observed that with increasing separation between the spheres the effect of pressure oscillation resulting from repeated reflections in the gap between the two particles decreases in magnitude.

Figure 7(d) shows the scattered force contribution for the third two-particle case, where the disturbing sphere is located laterally at a separation of 1.5 diameters. The effect of the scattered field on the drag force is substantial even in the case of the side-by-side arrangement. However, the scattered field of a neighbor appears to have a stronger influence on the drag force of a downstream particle than on a laterally displaced particle. It must be noted that while the peak in Fig. 7(c) remains narrow and negative, the corresponding perturbation force in Fig. 7(d) is positive and extends over a longer time. The drag force in Fig. 7(d) is significantly smaller than in Fig. 7(c) since the reference particle in the side-by-side configuration happens to be in a region where the disturbance changes sign (this will be evident later in Section IV A). Furthermore, as we will see below, in the lateral case, the reference particle experiences a substantial lift force. The increase in total drag in the lateral case is due to the blockage effect of the neighbor. The oscillations seen in the PR simulation are due to the repeated reflection of waves between the two particles. The C-MRG model recovers the force trend quite well, however, as can be expected, it does not account for the oscillations arising from the wave reflections between the two particles. With the increasing lateral separation between the two particles, we can expect the oscillation amplitude to decrease and the comparison to improve.

The C-MRG model allows for the separation of the force due to the incident shock and the scattered field into (i) undisturbed flow and (ii) inviscid unsteady contributions (i.e, separate the two terms of the right-hand side of (12)). Also plotted in Fig. 7 are time evolution of $\boldsymbol{F}_{un}$ and $\boldsymbol{F}_{iu}$. Frame (a) shows the undisturbed flow and inviscid unsteady contributions of the primary shock. Those due to the scattered field of the disturbing neighbor are presented in the other three frames. The sum of the two contributions is the C-MRG model prediction denoted as F^{in} in frame (a) and as F^{sc} in the other three frames. In all cases, the undisturbed flow and inviscid unsteady contributions are comparable in magnitude. Only for a very short duration immediately following the arrival of the scattered field, the two contributions reinforce each other to create a strong negative peak in the inline cases. At later times, the two contributions oscillate, but in a phase-shifted manner. Nevertheless, especially from frame (c), it is clear that both these contributions are needed to explain the effect of the scattered field.

In the drag force experienced by the side-by-side case in Fig. 7(d), it is interesting to point out that during the interval $0 \leq t - t_{sc} \leq \tau_{ps}$ the behavior of both components resembles Fig. 7(a), which suggests that the effect of the scattered field is essential to reinforce the strength of the incident shock, although with a time delay of t_{sc}. This reinforces the intuitive expectation that the blockage effect of the side-by-side neighbor increases the post-shock flow. This simple augmentation of the streamwise flow remains accurate only for a short duration after which the time evolution of the force contributions is complex. Also, the scattered field propagating in the y-direction will contribute to a lift force, which we shall consider below.

2. *Finite shock comparison*

We now investigate the accuracy of the C-MRG model and the superposition given in (13) at higher shock intensities. The two inline configurations presented in Fig. 8 are now considered at progressively higher shock Mach numbers of $M_s = 1.1$, 1.22 and 1.55. The comparison of drag forces obtained from PR simulations and predicted by the C-MRG model are presented in Fig. 8. In the limit of shock Mach number being close to unity, the post-shock incident flow and the scattered fields are close to the acoustic limit. Thus, in this limit, the error in C-MRG prediction arises from two main factors: (i) the limitation of C-MRG not accounting for the wave interactions between the two particles and (ii) any numerical error in approximating the scattered field and in the evaluation of convolution integrals of the C-MRG equation. When the incident shock is of finite amplitude (i.e., $M_s > 1$), there are additional sources of error that arise from the non-linear nature of the resulting flow. The acoustic scattering field is now only an approximation. It can be seen that the C-MRG model reasonably captures the behavior of the force contribution on the reference particle due to the scattered field, although the difference between the prediction and the PR simulation result tends to increase with M_s. The primary differences are again the amplitude of the negative peak as well as the positive peak that follows. The finite Mach numbers prediction can be improved by (i) improving the representation of the

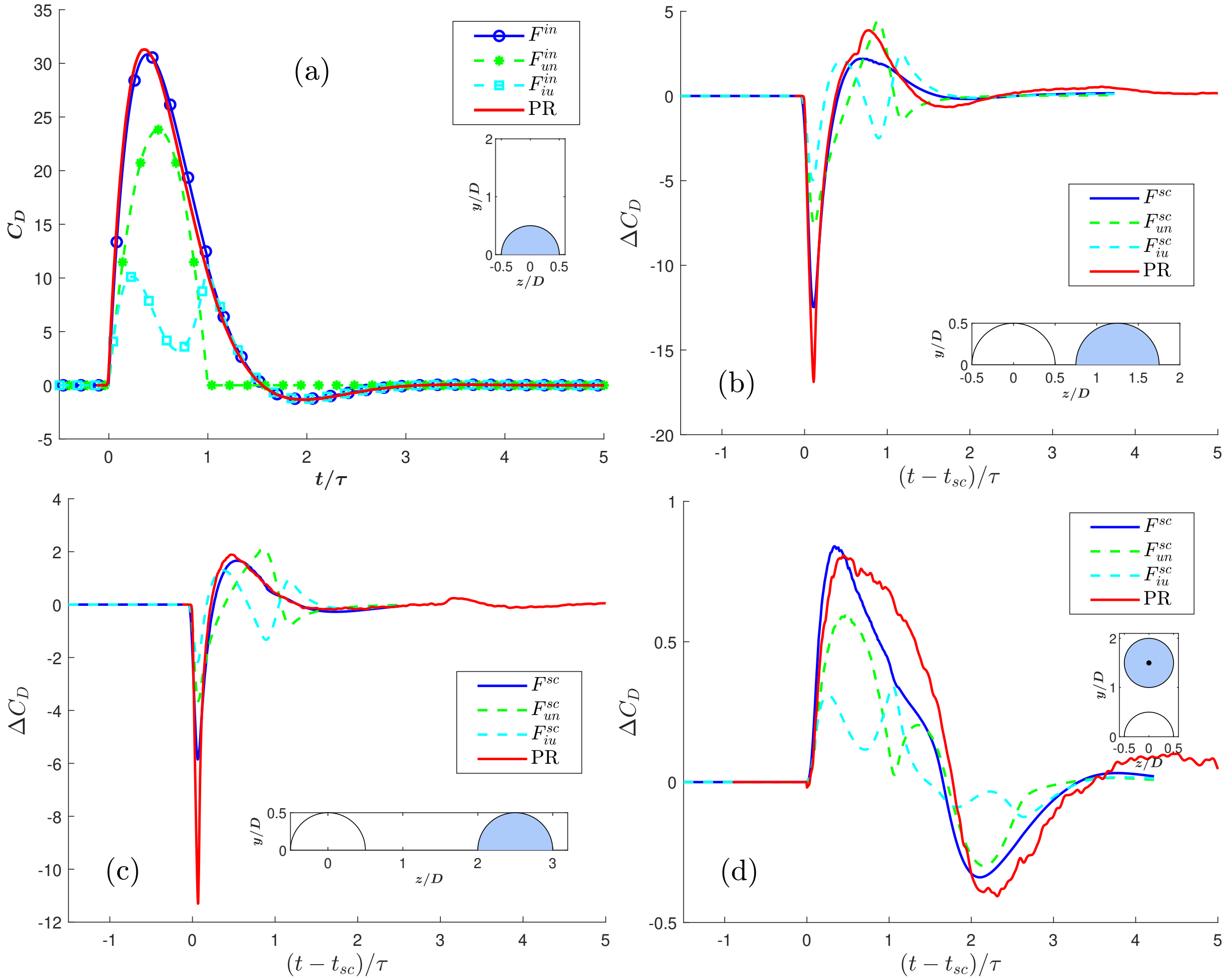

FIG. 7. Normalized drag force experienced by the reference particle as a planar shock passes over it, plotted as a function of time-shifted by the time of shock arrival and normalized by τ. In each case, the PR simulation result is compared against C-MRG prediction for $M_s = 1.05$. (a) Force on an isolated particle. (b) Force contribution of only the scattered field due to an upstream neighbor located inline with its center 1.25 D upstream of the center of the reference particle. (c) Scattered flow force due to an inline neighbor located 2.5 D upstream. (d) Drag force due to the scattered field of a neighbor located 1.5 D to the lateral side. In all four cases, the individual components in terms of the undisturbed flow force $\boldsymbol{F}_{un}$ and the inviscid unsteady force $\boldsymbol{F}_{iu}$ are also shown.

undisturbed flow of the reference particle beyond the acoustic approximation, (ii) adapting the C-MRG model to finite Mach numbers with improved kernels, and (iii) accounting for the effect of wave reflections between the particles. Also, we point out that the magnitude of the normalized force decreases with the Mach number since the forces are normalized by the post-shock velocity and post-shock density. The stronger the shock is, the stronger the post-shock conditions are, thus lowering the normalized force magnitude.

In the two inline cases, the effect of the scattered field only alters the drag force of the reference particle. Due to axisymmetry, the lateral force remains zero. In contrast, in the case of shock propagation over two size-by-side particles, the influence of the neighbor will not only alter the drag force as seen in the previous figures but will also introduce a non-zero transverse force. Figure 9 presents the normalized transverse force as a function of normalized and shifted time for the Mach number cases of $M_s = 1.05$ and 1.55. Note that the incident planar shock has no direct contribution to the lateral force and as a result, the entire lateral force is due to the scattering effect of the neighbor. Also plotted in each figure are $\boldsymbol{F}_{un}$ and $\boldsymbol{F}_{iu}$ components of the lateral force. t_{sc} adequately captures the timing of the rise of the lateral force. The values of the first peak in the lateral force shown in frame (a) compared to the drag contribution observed in Fig. 7(d) is larger since the reflected shock emitted from the disturbing sphere primarily travels in the transverse direction.

The lift force for the stronger $M_s = 1.55$ shock is shown in Fig. 9(b). The agreement is only qualitative, there are quantitative differences between the simulated force and the model prediction. Although the amplitude of the lateral force variation is reasonably predicted, it can be observed that there is a time shift that appears to increase. This

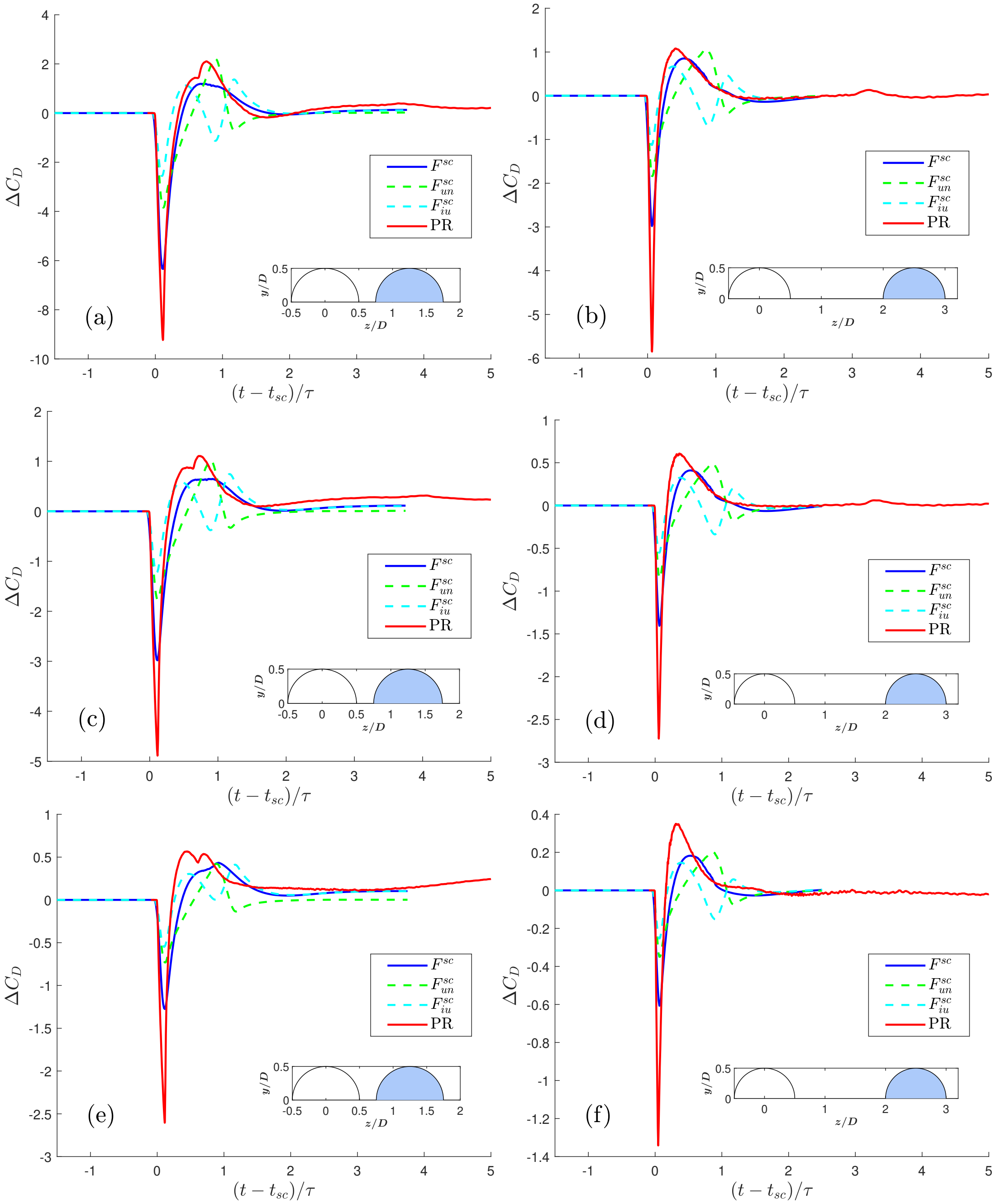

FIG. 8. Normalized drag force experienced by the reference particle as a planar shock passes over it. In each case, the PR simulation result is compared against C-MRG prediction and the force contribution of only the scattered field is presented. Frames (a) and (b) are for $M_s = 1.1$. Frames (c) and (d) are for $M_s = 1.22$. Frames (e) and (f) are for $M_s = 1.55$. Frames (a), (c), and (e) are for an inline configuration where the two particle centers are separated by $1.25D$. Frames (b), (d), and (f) are for an inline configuration where the two particle centers are separated by $2.5D$.

behavior can also be observed in frame (a), although the shift there is smaller. The C-MRG model evaluated with the acoustic approximation of the scattered flow assumes the disturbance to travel at the ambient speed of sound, whereas the disturbance waves from the finite Mach shock are expected to travel differently. The disturbance must arrive at a lateral location while being advected downstream by the finite Mach number flow. This has the effect of slowing down the effective velocity in the lateral direction due to the Doppler effect.

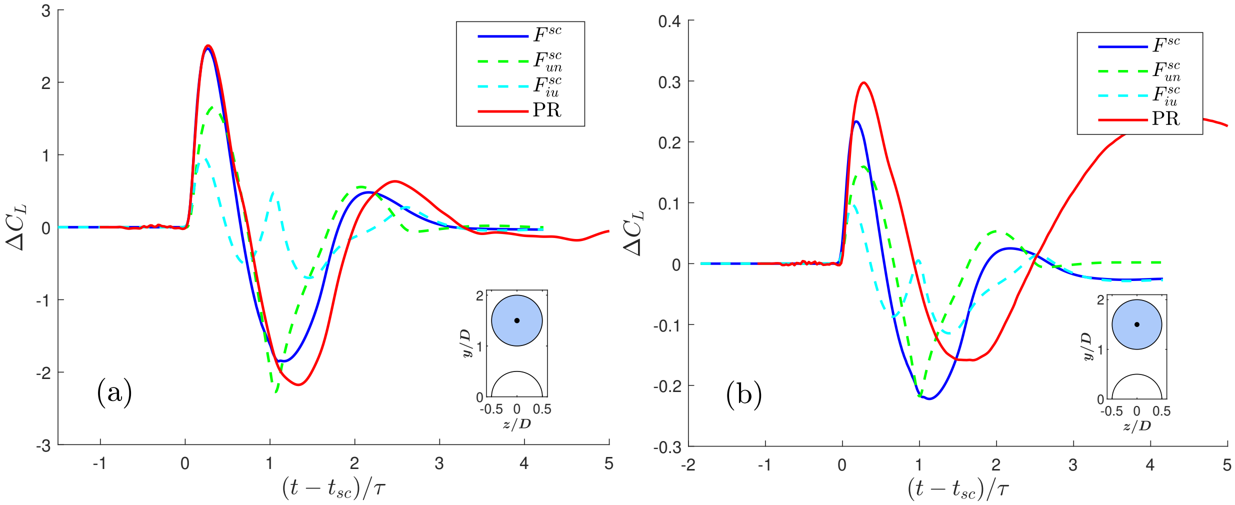

FIG. 9. The normalized lateral force experienced by the reference particle as a planar shock passes over the side-by-side particle pair. In each case, the PR simulation result is compared against C-MRG prediction. (a) $M_s = 1.05$ and (b) $M_s = 1.55$.

IV. C-MRG MODEL WITH PAIRWISE SUPERPOSITION

We now proceed to extend the above analysis to a distribution of particles subjected to a planar shock, similar to those considered in several recent investigations [9, 23, 25, 38, 41, 42, 57]. We will again consider the situation where the particles are held stationary during the shock propagation, which is a reasonable assumption in the limit when particle density is much larger than the gas density and when attention is focused on the short time immediately following shock propagation. In evaluating the force, each particle within the distribution, one at a time, must be considered as the reference particle. The chosen reference particle will then be subjected to the incident planar shock plus the scattered flow of its neighbors. Under the pairwise interaction assumption [2, 3, 39], the perturbation flow induced by the collective action of all the neighbors is represented as a sum of perturbations (or scattered field) due to individual neighbors. This pairwise superposition of the undisturbed flow of the reference particle can be represented as

$$\begin{aligned} \overline{p^{un}\boldsymbol{n}}^s &= \overline{p^{in}\boldsymbol{n}}^s + \sum_{j=1}^{J} \overline{p^{sc}_j \boldsymbol{n}}^s\,, & \overline{(\rho\boldsymbol{u})^{un}}^s &= \overline{(\rho\boldsymbol{u})^{in}}^s + \sum_{j=1}^{J} \overline{(\rho\boldsymbol{u})^{sc}_j}^s\,, \\ \overline{(\rho\boldsymbol{u}_r)^{un}}^s &= \overline{(\rho\boldsymbol{u}_r)^{in}}^s + \sum_{j=1}^{J} \overline{(\rho\boldsymbol{u}_r)^{sc}_j}^s\,, & \overline{\boldsymbol{u}^{un}_r}^s &= \overline{\boldsymbol{u}^{in}_r}^s + \sum_{j=1}^{J} \overline{\boldsymbol{u}^{sc}_{r,j}}^s\,. \end{aligned} \tag{14}$$

In the above, the index j corresponds to the j^{th} neighbor of the reference particle. The sum from 1 to J is intended to cover the influence of all the neighbors, with $j = 1$ corresponding to the closest neighbor, $j = 2$ the second closest, and so on. Typically J can be restricted to $O(10)$ since neighbors that are closest to the reference particle are expected to have the greatest influence.

In the above superposition, we intend to approximate the pressure, density, and velocity perturbations of the j^{th} neighbor in terms of the acoustic approximation to the scattering of the propagating shock presented in section II. The superposition is only an approximation for the following reasons. First, the scattered fields considered in section II are the disturbance fields created by an isolated particle subjected to a planar shock. In the present case, each neighbor is not subjected to a perfect planar shock. Each neighbor in fact encounters a shock that is modified by the perturbations induced by all its neighbors. Second, while the scattered field of the nearest neighbor may arrive at the reference particle relatively unaffected by the presence of all other distant particles, the same is not true of the scattered field of distant neighbors. The scattered field from a neighbor that is farther away may be modified by other closer neighbors before it arrives at the reference particle. Third, the acoustic approximation ignores the non-linear nature of finite amplitude shock. In essence, these approximations will influence the accuracy of the undisturbed flow and the resulting force evaluation. Nevertheless, for lack of any better theoretical approach, we proceed with the linear assumption implicit in the pairwise superposition, ignoring non-linear interactions presented by the N-body problem.

A. Perturbation Maps

The advantage of the pairwise interaction approximation is that the perturbing pressure and velocity influence of a neighbor can be pre-computed and stored. In particular, the surface averages contained in quantities $-S_p\overline{p\boldsymbol{n}}^S$, $\partial\overline{(\rho\boldsymbol{u}_r)}^S/\partial t$, $\overline{\rho\boldsymbol{u}}^S$, and $\nabla\overline{\boldsymbol{u}_r}^S$ that appear in the C-MRG equation given in (12) can be computed and stored as fields. These fields are functions of time, and also depend on $\boldsymbol{x}_P$ the relative location of the reference particle with respect to the disturbing neighbor (which is taken to be located at the origin). Since the scattered field of the disturbing neighbor is axisymmetric, the variation of $\boldsymbol{x}_P$ only over the upper half of the $y-z$-plane needs to be considered.

The map of the streamwise component of $-S_p\overline{p\boldsymbol{n}}^S$ at six different time instances normalized by τ is presented in the upper half of each frame of Fig. 10. The map must be interpreted in the following manner. For any chosen point within the contour, for a reference particle that is centered at that point, the streamwise component is given by the contour level, which according to (12) is equal to the undisturbed flow drag. The black region is the disturbing particle and the white annular band around it corresponds to the region within which the center of the reference particle cannot lie since the distance between the two particles cannot be less than one particle diameter. Outside this band of the excluded region, the maps are created with 31 radial positions discretizing $|\boldsymbol{x}_p|/D$ from 1.025 to 4 and 81 angular positions. The maps are also resolved with 501 time instances extending from $-\tau$ to 5τ, where zero time corresponds to when the incoming shock first touches the black disturbing sphere.

The corresponding transverse component of $-S_p\overline{p\boldsymbol{n}}^S$ is shown in the lower half of each frame of Fig. 10. The outward propagating waves contributing to positive and negative fluctuations can be seen in both the streamwise and transverse components. The temporal decay of the emanating waves from the disturbing sphere is clear. Also, it can be seen that the intensity of the first train of positive and negative regions (i.e., the intensity of blue and red regions) decreases over time. As a result, as can be expected, the influence of the disturbing sphere (shaded black) on the reference particle depends on the distance. With increasing distance, the undisturbed flow force on the reference particle will decrease. From the spatial structure of the contours, it can be noted that the undisturbed flow drag due to the scattered field is relatively low for a reference particle that is located laterally with its center near the $z=0$ plane, since the waves happen to change sign near this plane, except at an early time and very close to the disturbing sphere. In contrast, the transverse component is zero along the $y=0$ plane and reaches a larger value to the lateral sides of the reference particle.

The corresponding contours of $\partial\overline{(\rho\boldsymbol{u}_r)}^S/\partial t$ are shown here in Fig. 11. Again six different time instances are shown and the upper and lower halves present the streamwise and transverse components. Again an outward propagating wave packet can be observed and due to the radial expansion of the packet, its intensity decreases over time. It must be cautioned that the contours shown in Fig. 10 directly correspond to streamwise and transverse force on the reference sphere, whereas, the contours shown in Fig. 11, only when weighted by the history kernel and integrated over past times, corresponds to inviscid unsteady force contribution due to temporal acceleration of the scattered field of the neighbor. Thus, the inviscid unsteady force contribution on the reference particle immediately after the arrival time of the scattered field will be negative and given by the contour value. However, with the passage of time, the time integration will receive contributions from past values of $\partial\overline{(\rho\boldsymbol{u}_r)}^S/\partial t$ as well and thereby damping the level of the force oscillation. As in the undisturbed flow force, here too, we observe the force to be lower along the $z=0$ plane. The maps of the other quantities are presented in the Supplemental Material [1]. From these sets of maps the perturbation of each neighbor can be calculated, which can then be added as given in (14) and substituted into the C-MRG model to obtain the force prediction.

B. Validation with PR Simulations

In this section, we will evaluate the capability of the C-MRG force model along with the pairwise superposition of the primary shock with the disturbance fields of the surrounding neighbors in predicting the time evolution of the force. In evaluating the surface average of the undisturbed flow seen by each particle, we will use the maps presented in the previous section for the perturbation of each neighbor. The model prediction will be compared against corresponding PR simulations of shock propagation over a random distribution of particles. In this section, $t=0$ corresponds to the first instance the shock touches the leading particle and τ is defined as D/u_s, where u_s is the velocity of the incident shock.

Results from two different PR simulations will be used for evaluating the C-MRG force model prediction. Both are randomly distributed particle beds of volume fraction 10% and the location of the particles is maintained identically the same in both simulations. The two cases use two different fluids, namely water and air. Both these datasets were previously considered by Behrendt et al. [9]. The Mach number of both cases is 1.22. The specification of the thermodynamic properties of the pre-shock region of the two datasets is tabulated in Table I. In the current C-MRG

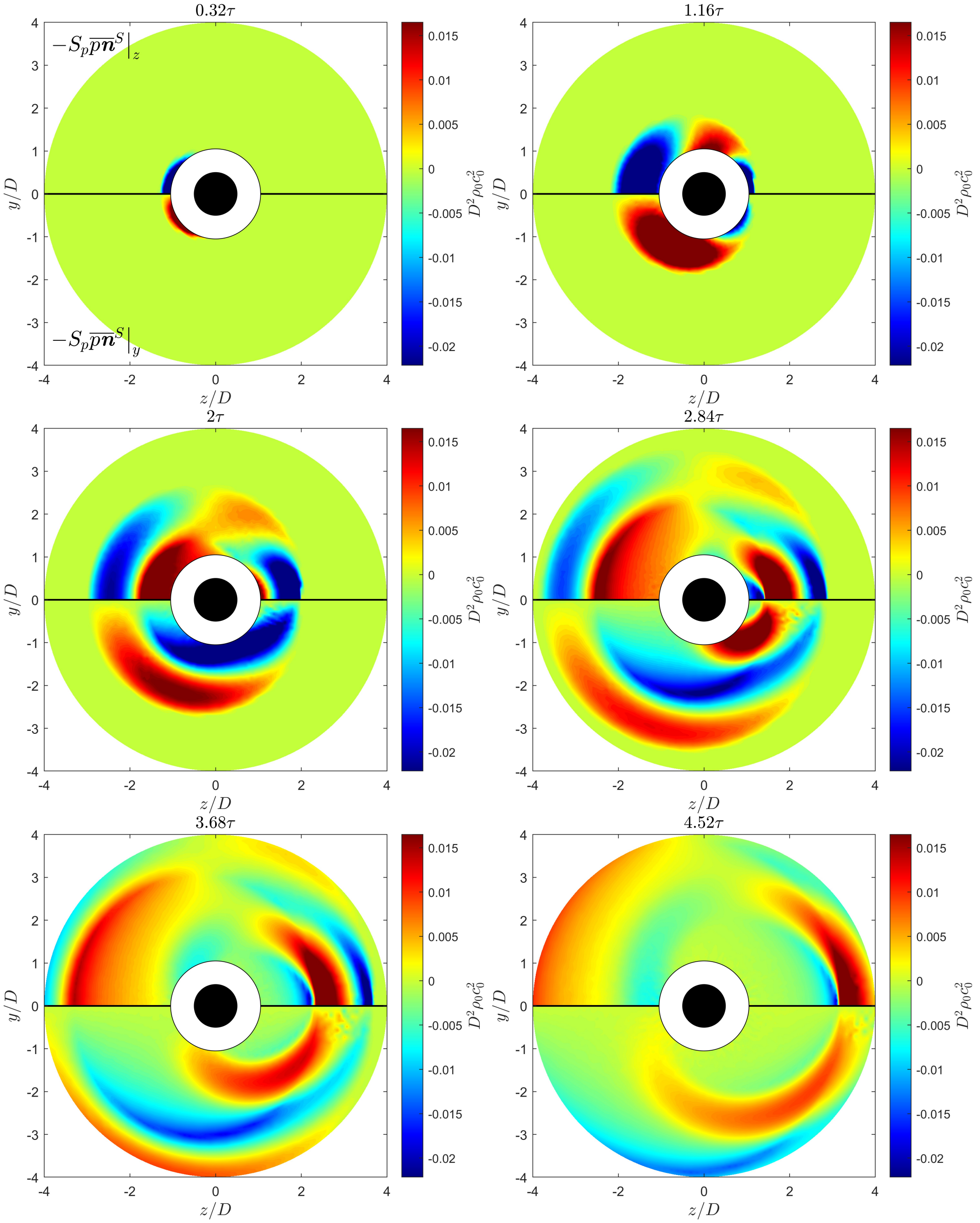

FIG. 10. $-S_p\overline{p\boldsymbol{n}}^S$ disturbance maps. The inner black half circle denotes the location of the disturbing particle and the region shaded in white denotes locations that the reference particle's center cannot reach. The upper half plots the streamwise component and the lower half plots the transverse component. $D^2\rho_0 c_0^2$ is the normalizing factor and the quantities plotted are noted in the first frame.

model, the inputs required to estimate the time-dependent force of a particle within the random bed are the pre- and post-shock fluid properties and the location of the particle and its immediate J neighbors. Perturbation maps computed at 200 time instances after shock arrival were used to calculate the scattered field of each of the J neighbors.

Figure 12 shows the time evolution of both the predicted force (blue line denoted as "PIEP") and the PR simulation result (red line denoted as "PR") for the case of water as the fluid medium. Also plotted in the figure as an orange dashed line is F^{in}, which corresponds to the force due to the primary incident shock alone without including the scattering effect of all the neighbors. Thus the difference between the red solid and orange dash line can be interpreted as the effect of neighbors in altering the force. In the case of particle numbered 11, shown in frame (a), the neighbors cause the peak force to increase above that of an isolated particle subjected to shock. Whereas in the case of particles numbered 57, 74, and 145 shown in frames (b), (c), and (d) the effect of neighbors decreases the magnitude of peak

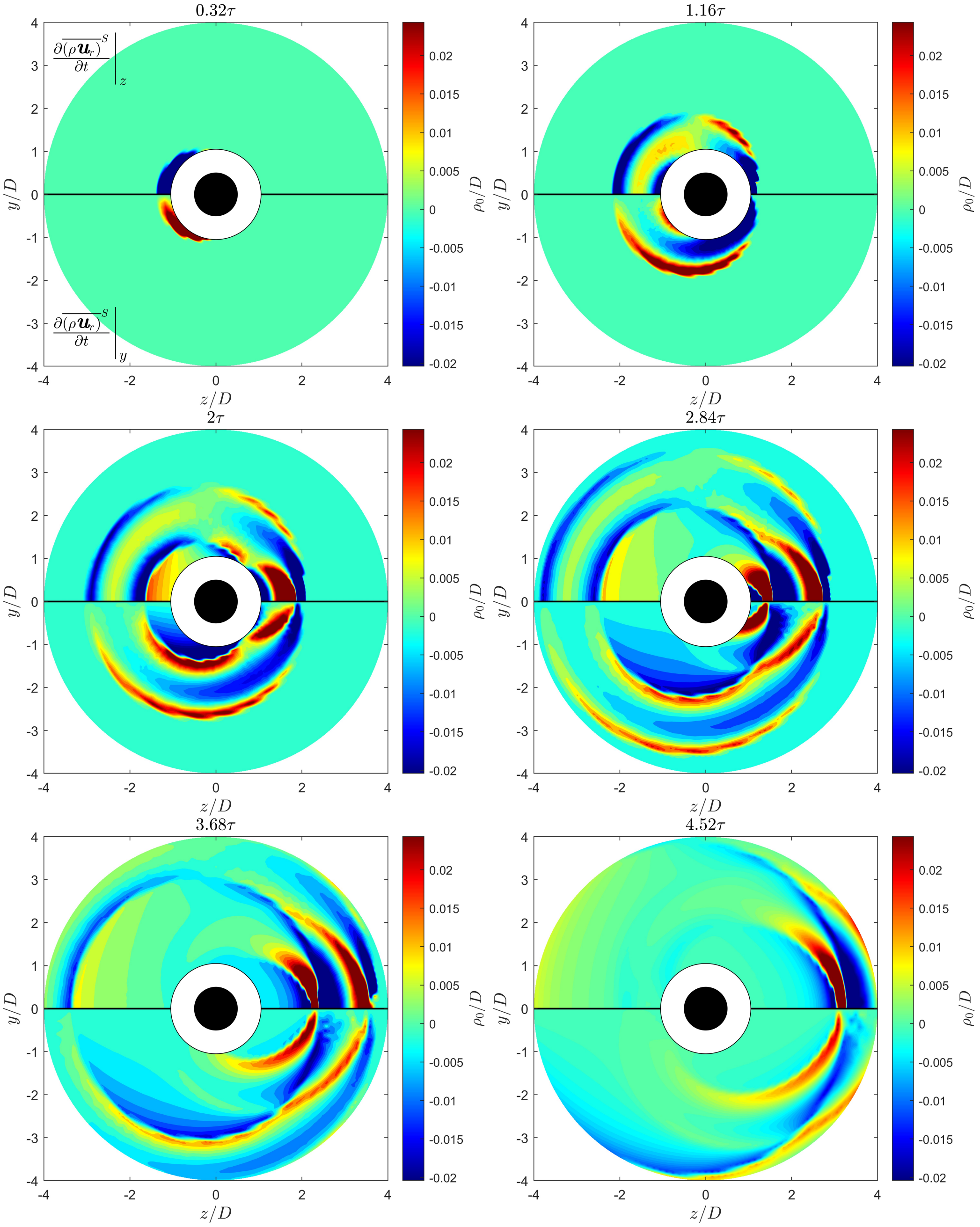

FIG. 11. $\frac{\partial \overline{(\rho \boldsymbol{u}_r)}^S}{\partial t}$ disturbance maps. The inner black half circle denotes the location of the disturbing particle and the region shaded in white denotes locations that the reference particle's center cannot reach. The upper half plots the streamwise component and the lower half plots the transverse component. ρ_0/D is the normalizing factor and the quantities plotted are noted in the first frame.

force and delays the time of the peak force relative to the time of arrival of the shock. It can be observed that the C-MRG model, although not perfect, can correctly identify the increase and decrease of the peak force by accounting for the constructive and destructive influence of the neighbors. The agreement between the simulation and C-MRG model prediction (red and blue curves) is quite good not only in predicting the dominant positive peak, but also the subsequent oscillations. Although, the frequency of predicted oscillation becomes increasingly higher than that obtained in the simulation at later times. Although not perfect, given the fact that there does not exist any other theory, the C-MRG model's prediction seems very encouraging.

Also plotted in each frame are two other results that correspond to the undisturbed flow force and the inviscid unsteady force on the particle. Each of these components is in turn made up of contributions from the primary

TABLE I. Values for the pre-shock ambient condition in the randomly packed PR simulations.

	p_0 (Pa)	ρ (kg/m^3)	c_0(m/s)
water	101325	998	343.21
air	101325	1.2041	1626.57

incident shock as well as scattering fields from the J immediate neighbors. It was observed in Fig. 7 that both the undisturbed flow force and the inviscid unsteady force components are important in accurately capturing the time evolution of force on an isolated particle subjected to a planar shock. It can be observed this conclusion remains valid even in the case of a random distribution of particles. Furthermore, the initial shape of these forces also remains qualitatively similar. Only their amplitude is altered and this results in the increase or decrease of the peak observed in the overall force.

Figure 13 shows the time evolution of force of two different particles in the case of air as the fluid medium. From the plots, it is clear that the C_D is substantially lower in the case of air (note that the actual force magnitude is expected to be far lower due to the lower density of air than water). Nevertheless, we observe the peak force on individual particles to be substantially higher or lower than that of an isolated particle. This clearly indicates the importance of the relative location of neighbors in influencing the local undisturbed flow to the force experienced by a particle. The C-MRG model is again able to capture the time evolution of force, including the magnitude and timing of the peak, quite accurately. Here, it should be noted that the PR simulation with water as the medium used the stiffened equation of state, while the simulation with air as the medium used the ideal gas law for the equation of state. Despite these differences in the equation of state, the C-MRG model is able to reasonably accurately account for the effect of neighbors. Of course, the comparison is only qualitatively good at later times. This is perhaps due to the use of the acoustic model and perhaps can be improved by evaluating the finite Mach number effect on the scattered fields.

We now proceed to evaluate the difference between the force evolution obtained in the PR simulation and the C-MRG model prediction for all the particles of the random bed. For such a comparison we use the peak value of the force as the comparison metric. The neighbors can influence the value of the peak force in different ways: if several neighbors directly block the reference particle by being on the upstream side, the reference particle will effectively see a weaker shock and therefore the peak shock value will be smaller. On the other hand, if there are disturbing spheres located upstream, but to one side, channel the flow between them towards the reference particle thus generating a larger peak drag [9]. Scatter plots of peak predicted force with the C-MRG model against the actual PR simulation peak force for water and air are shown in Fig. 14. In both cases, the mean drag averaged over all the particles has been subtracted, since it has been shown to be dictated by the average shock strength as it passes through the bed [9]. Thus the focus is on the model's ability to predict whether a particle will experience a higher- or lower-than-average force based on the influence of its neighbors. It is clear from the scatter plots that the model is not perfect, for otherwise in a perfect model all the data points would have fallen along the 45° line. Nevertheless, it is quite clear that the model can identify those particles whose peak force is substantially larger or smaller than the mean. The correlation coefficient for the case of water is 0.558 and for air is 0.587. In fact, we can partition the 200 particles within the bed into four sections - upstream, left-of-center, right-of-center, and downstream sub-slabs of particles, each containing about 50 particles. In the most upstream section of the bed, the strength of the primary incident shock remains unaffected, while in the subsequent sections the incident shock seen by the particles is modified (weakened) by the upstream particles. Since the model assumes the incident shock to remain unaffected, it can be expected that the model performance is likely to be at its best in the upstream section. The correlation coefficient calculated only with the upstream particles yields 0.767 and 0.805 for water and air, respectively. It should also be pointed out that comparisons between the PIEP model prediction and PR results in the incompressible regime for steady flow over a random distribution of particles yielded similar results, where the model is not perfect, but was able to capture a significant portion of the actual trend [2].

We then consider the time gap between when the peak drag force is reached and the earlier moment when the leading shock first touches the particle. The difference between the simulation result and the model prediction of the time gap is shown in Fig. 15 for all the particles as a function of their axial location. The results for both water and air are shown. The timing is captured well for the first few particles in the bed and as the depth z increases, the delay goes larger, and the difference is more severe for the air shock case compared to the water shock case. Behrendt et al. [9] provided similar findings, as the shock front strength decreases faster for an air shock compared to a water shock going through the particle bed. In the current model, we assume the shock strength to be constant, regardless of its axial location. In reality, the disturbing spheres see disturbed and deformed shock fronts. These secondary interactions are not considered in the model.

Another important effect of neighbors is that they prolong the duration of force fluctuation due to wave reflections between the particles. In the case of an isolated particle shown in Fig. 7(a), the force oscillations die out rapidly in

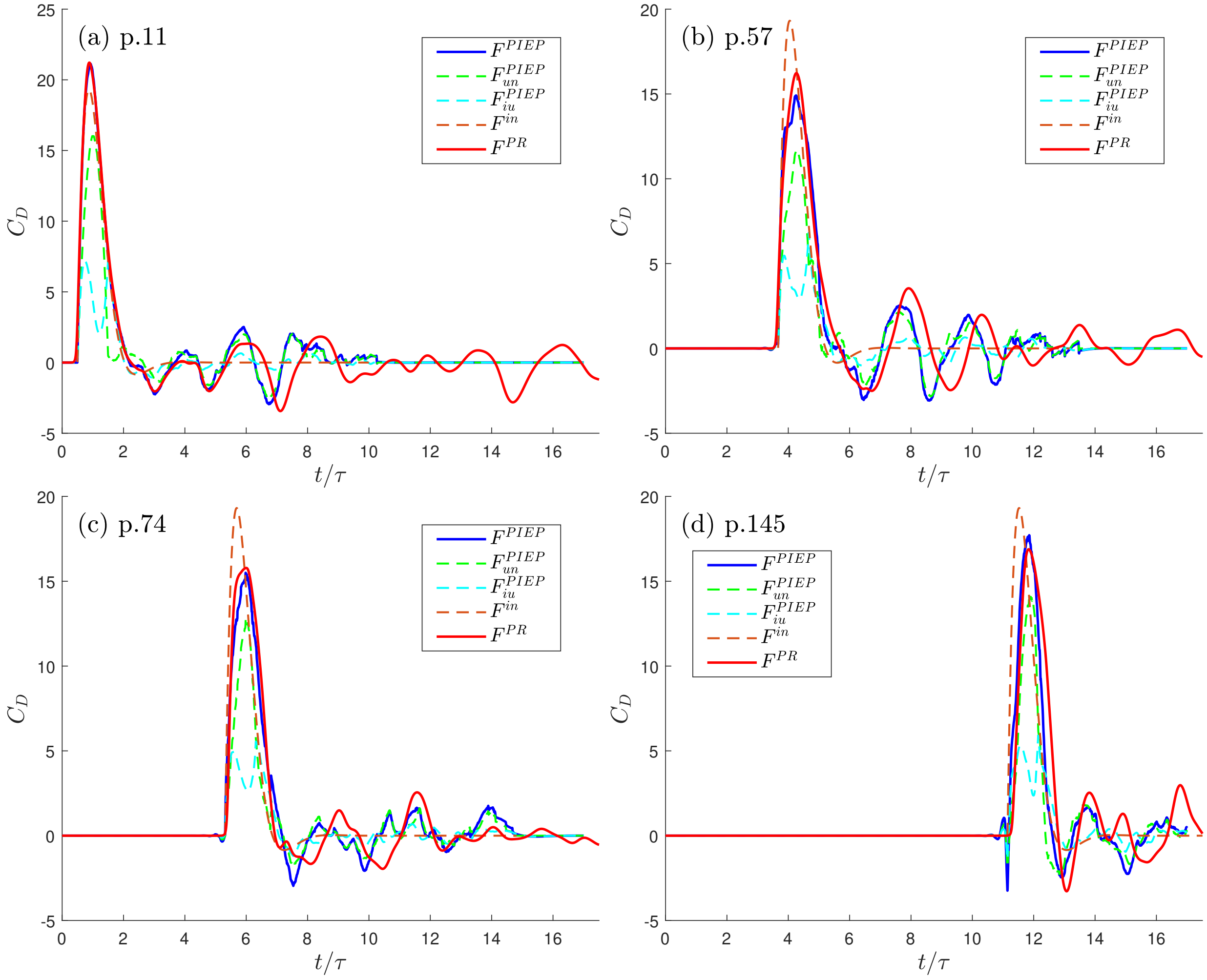

FIG. 12. Unsteady force comparison between PR simulation (red) and prediction using the C-MRG model (blue) for a water shock through the particle bed. The orange curve is the force experienced by that particle without any neighboring disturbances, subject to a pure shock. The green curve is the undisturbed contribution and the cyan curve is the inviscid unsteady contribution. The streamwise location for each of the particle center is: p.11 - 1.00D, p.57 - 4.17D, p.74 - 5.81D, and p.145 - 11.65 D.

contrast to force fluctuations seen by the different particles seen in Fig. 12. This can be quantified in terms of rms force fluctuation F_{rms}, which is computed by taking rms of the force oscillation within a time window for each of the particles. The start of this time window is when the primary shock passes the particle and the force crosses zero and the end of the time window is 9τ, after the moment the primary shock touches the reference sphere. The rms force fluctuation of the different particles can then be averaged to obtain $\langle F_{rms}\rangle$. The average rms force fluctuation obtained from the PR simulation is compared with that predicted by the model in Table II for both water and air. Also shown for comparison is that of an isolated particle. The magnitude of the oscillation for water is larger than that for air, as in general F^{in} is higher in magnitude. Compared to the small post-shock oscillation values observed in F^{in}_{rms}, $\langle F^{PR}_{rms}\rangle$ is significantly larger, and the C-MRG model is able to capture the increased force fluctuations due to neighbor interactions. Since the current model only considers the effect of disturbing particles on a reference particle, the secondary effects such as wave reflection between the particles are ignored. These secondary reflections tend to create more force oscillation contributing to enhanced pseudo-turbulence. Hence it is to be expected that $\langle F^{PR}_{rms}\rangle$ is larger than $\langle F^{PIEP}_{rms}\rangle$. It is also interesting to observe that PIEP prediction is closer to PR results in the case of water due to perhaps reduced compressibility effects and wave reflections.

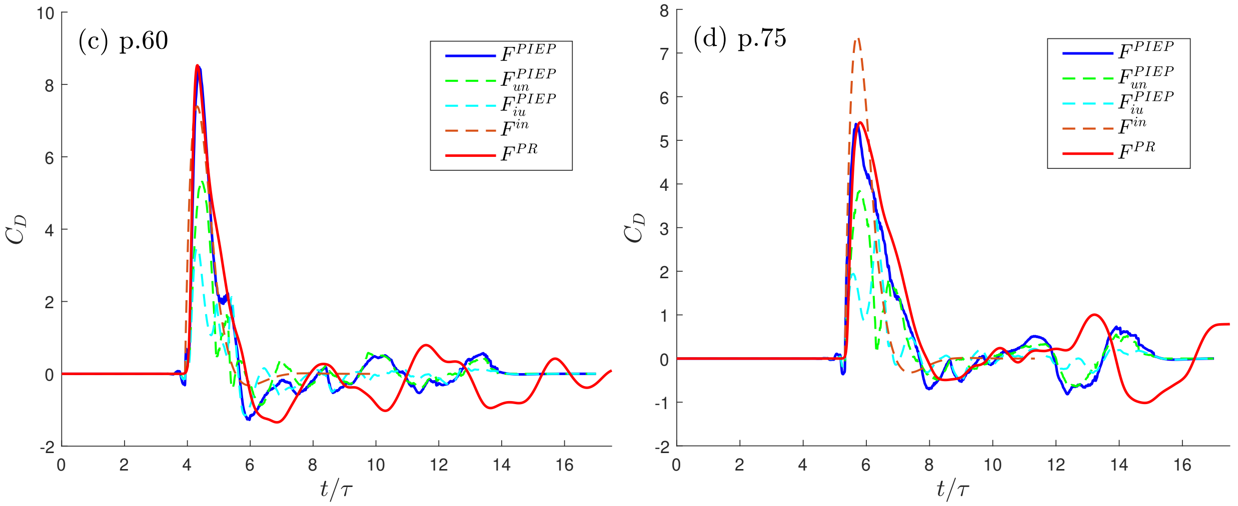

FIG. 13. Unsteady force comparison between PR simulation (red) and prediction using the C-MRG model (blue) for an air shock through the particle bed. The orange curve is the force experienced by that particle without any neighboring disturbances, subject to a pure shock. The green curve is the undisturbed contribution and the cyan curve is the inviscid unsteady contribution. The streamwise location of the particle centers are: p.60 - 4.42D, and p.145 - 5.82 D.

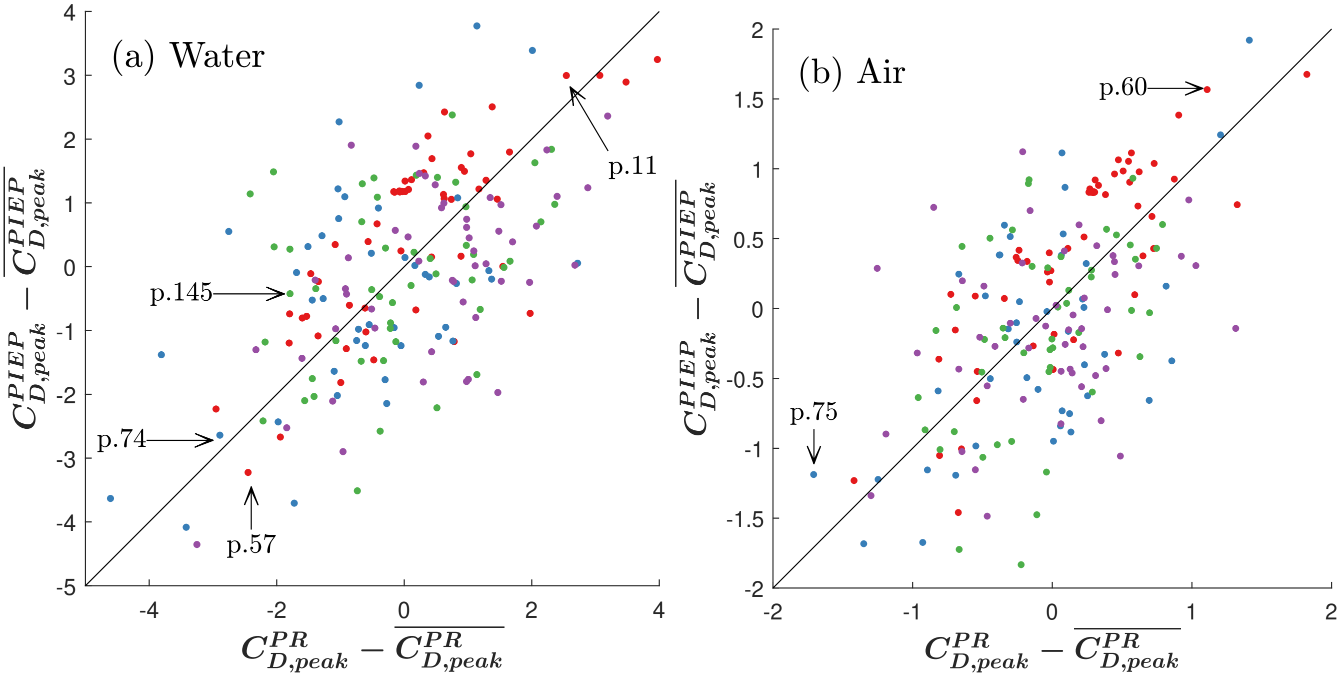

FIG. 14. Peak force comparisons for the case of (a) water and (b) air shock. Each of the points is colored corresponding to the quarter in which the center is located. Colors red, blue, green, and purple correspond to upstream, left-of-center, right-of-center, and downstream sections of the bed. Several particles are highlighted in each figure and the force curves experienced by these particles are shown in Figures 12 and 13. The mean peak drag has been subtracted: $C_{D,peak}$ denotes the peak value for each particle and the overline $\overline{()}$ denotes the average value.

V. CONCLUSIONS

As a planar shock propagates through a randomly placed particle bed, it is observed that in addition to the transmitted shock and the waves reflected by the upstream edge of the bed, there are distorted compression and rarefaction waves that linger within the particle bed. Aside from using PR simulation to study common systems as such in nature, existing force models consider only individual particles interacting with the shock. In this work, we construct a framework to account for the particle-wave-particle interaction by extending the incompressible pairwise

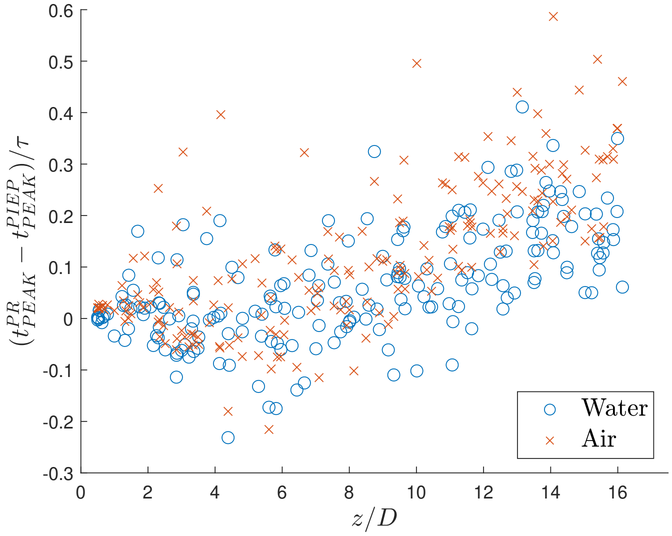

FIG. 15. The time delay between when the drag force in PR simulation reaches the maximum and that predicted by the model. The horizontal axis is the depth in z where the particles sit and the vertical axis is the time delay observed. The blue circles denote results for the water shock case and the red crosses are for the air shock case.

TABLE II. Rms values of post-shock oscillation for PR-simulation (superscript ^{PR}) and the model (superscript ^{PIEP}).

	F^{in}_{rms}	$\langle F^{PR}_{rms} \rangle$	$\langle F^{PIEP}_{rms} \rangle$
Water	0.2366	1.4193	1.1660
Air	0.0980	0.6442	0.4278

interaction extended point-particle (PIEP) approach to the unsteady compressible regime.

A classical solution of scattering acoustic waves from a hard sphere is utilized to reconstruct the flow field due to a moving shock. We established the accuracy of a numerical evaluation of the analytical spherical harmonics solution to model the flow field by comparing it with the results of a PR simulation of a single sphere subject to a planar shock. In the process, we formulated relations for the timing of the scattered shock signal to arrive using the Huygens-Fresnel principle. To step-by-step verify the validity of the compressible Maxey-Riley-Gatignol (C-MRG) force model in conjunction with the acoustic scattering theory, two-sphere force predictions are compared to corresponding two-particle PR simulations subjected to a planar shock. It is observed that even though higher-order wave interactions between the two particles are not considered, the C-MRG model predicts well the time evolution of the drag and lift forces, even at finite shock Mach numbers.

We store the key components of the C-MRG force expression as influence maps in the form of data libraries and investigate the superposition assumption by reading the maps to obtain the individual influence of each neighbor and sum up the influences to approximate the force components of a reference particle. The C-MRG model is computed with the approximate undisturbed flow fields to obtain the force prediction. Since the force is time-dependent we use the peak force as the shock propagates over a particle as the proxy to the time evolution and analyze the peak predictions of the drag forces compared to PR simulation. This comparison is made for both water and air as the surrounding fluid for a randomly packed particle bed at a volume fraction of 10 %. It is observed that the model captures well the particle-to-particle peak drag variation based on the location of the neighboring particle. The effectiveness of the model slightly decays as the shock front is deeper into the bed, as the shock front seen by each disturbing neighboring sphere is more deformed. This effect is more severe in the air shock system compared to the water shock system. The model is also capable of predicting the persistent drag oscillations from disturbance waves bouncing between the particles even after the passage of the primary shock. Thus the C-MRG model pairwise superposition of the scattering of the neighbors is a cost-effect computational method to resolve the particle forces in EL simulations. As future work, it will be interesting to consider a larger range of volume fractions of the dispersed phase and Mach numbers to investigate the limit of this pairwise interaction model.

ACKNOWLEDGEMENTS

SH and SB gratefully acknowledge support from Lawrence Livermore Laboratory as part of their LDRD funding (Grant no. B633900). The work was also supported by the US Department of Energy, National Nuclear Security Administration under SSAA GRANT 13433012 and the Predictive Science Academic Alliance Program, Contract No. DE- NA0002378. This work was performed under the auspices of the U.S. Department of Energy by Lawrence Livermore National Laboratory under Contract DE-AC52-07NA27344. LLNL-JRNL-842816-DRAFT. SH would also like to acknowledge Sam Briney for the technical expertise in the optimization of simulations.

---

[1] `URL_will_be_inserted_by_publisher`.

[2] G Akiki, TL Jackson, and S Balachandar. Pairwise interaction extended point-particle model for a random array of monodisperse spheres. *Journal of Fluid Mechanics*, 813:882–928, 2017.

[3] Georges Akiki, WC Moore, and S Balachandar. Pairwise-interaction extended point-particle model for particle-laden flows. *Journal of Computational Physics*, 351:329–357, 2017.

[4] Subramanian Annamalai and S Balachandar. Faxén form of time-domain force on a sphere in unsteady spatially varying viscous compressible flows. *Journal of Fluid Mechanics*, 816:381–411, 2017.

[5] S Balachandar. Lagrangian and eulerian drag models that are consistent between euler-lagrange and euler-euler (two-fluid) approaches for homogeneous systems. *Physical Review Fluids*, 5(8):084302, 2020.

[6] S Balachandar and Kai Liu. A correction procedure for self-induced velocity of a finite-sized particle in two-way coupled euler–lagrange simulations. *International Journal of Multiphase Flow*, 159:104316, 2023.

[7] S Balachandar, Kai Liu, and Mandar Lakhote. Self-induced velocity correction for improved drag estimation in euler–lagrange point-particle simulations. *Journal of Computational Physics*, 376:160–185, 2019.

[8] Jacob Behrendt, S Balachandar, Joshua Garno, and Thomas P McGrath. Modeling of shock-induced force on an isolated particle in water and air. *Physics of Fluids*, 34(1):016108, 2022.

[9] Jacob Behrendt, S Balachandar, and TP McGrath. Shock interacting with a random array of stationary particles underwater. *Physical Review Fluids*, 7(2):023401, 2022.

[10] Luca Brandt and Filippo Coletti. Particle-laden turbulence: progress and perspectives. *Annual Review of Fluid Mechanics*, 54:159–189, 2022.

[11] Jesse Capecelatro. Modeling high-speed gas–particle flows relevant to spacecraft landings. *International Journal of Multiphase Flow*, page 104008, 2022.

[12] Jesse Capecelatro and Olivier Desjardins. An euler–lagrange strategy for simulating particle-laden flows. *Journal of Computational Physics*, 238:1–31, 2013.

[13] Matteo Chiesa, Vidar Mathiesen, Jens A Melheim, and Britt Halvorsen. Numerical simulation of particulate flow by the eulerian–lagrangian and the eulerian–eulerian approach with application to a fluidized bed. *Computers & Chemical Engineering*, 29(2):291–304, 2005.

[14] TJB Collins, A Poludnenko, A Cunningham, and A Frank. Shock propagation in deuterium-tritium-saturated foam. *Physics of Plasmas*, 12(6):062705, 2005.

[15] Clayton T Crowe. *Multiphase Flow Handbook*. CRC press, 2005.

[16] Renée Gatignol et al. The faxén formulae for a rigid particle in an unsteady non-uniform stokes flow. *JOURNAL DE MECANIQUE THEORIQUE ET APPLIQUEE*, 2(2), 1983.

[17] Paolo Gualtieri, F Picano, Gaetano Sardina, and Carlo Massimo Casciola. Exact regularized point particle method for multiphase flows in the two-way coupling regime. *Journal of Fluid Mechanics*, 773:520–561, 2015.

[18] Takahi Hasegawa and Katuya Yosioka. Acoustic-radiation force on a solid elastic sphere. *The Journal of the Acoustical Society of America*, 46(5B):1139–1143, 1969.

[19] Andreas Haselbacher. Rocflump developer's guide, 08 2003.

[20] Andreas Haselbacher. A weno reconstruction algorithim for unstructured grids based on explicit stencil construction. In *43rd AIAA Aerospace Sciences Meeting and Exhibit*, page 879, 2005.

[21] Cambridge Horace Lamb, Trinity College. *Hydrodynamics*. Cambridge University Press, 1993.

[22] JAK Horwitz and Ali Mani. Accurate calculation of stokes drag for point–particle tracking in two-way coupled flows. *Journal of Computational Physics*, 318:85–109, 2016.

[23] Zahra Hosseinzadeh-Nik, Shankar Subramaniam, and Jonathan D Regele. Investigation and quantification of flow unsteadiness in shock-particle cloud interaction. *International Journal of Multiphase Flow*, 101:186–201, 2018.

[24] Peter J Ireland and Olivier Desjardins. Improving particle drag predictions in euler–lagrange simulations with two-way coupling. *Journal of Computational Physics*, 338:405–430, 2017.

[25] Rahul Babu Koneru and S Balachandar. An assessment of the drag models in the case of a shock interacting with a fixed bed of point particles. *Journal of Fluids Engineering*, 143(1):011401, 2021.

[26] Stuart Laurence and Ralf Deiterding. Shock-wave surfing. *Journal of Fluid Mechanics*, 676(06):1–36, 2011.

[27] Stuart J Laurence, Ralf Deiterding, and G Hornung. Proximal bodies in hypersonic flow. *Journal of Fluid Mechanics*, 590:209–237, 2007.

[28] Vyacheslav Ivanovich Lebedev. Quadratures on a sphere. *USSR Computational Mathematics and Mathematical Physics*, 16(2):10–24, 1976.

[29] Y Ling, JL Wagner, SJ Beresh, SP Kearney, and S Balachandar. Interaction of a planar shock wave with a dense particle curtain: Modeling and experiments. *Physics of Fluids*, 24(11):113301, 2012.

[30] C Lu, S Sambasivan, A Kapahi, and HS Udaykumar. Multi-scale modeling of shock interaction with a cloud of particles using an artificial neural network for model representation. *Procedia IUTAM*, 3:25–52, 2012.

[31] Adam A Martinez, Gregory C Orlicz, and Katherine P Prestridge. A new experiment to measure shocked particle drag using multi-pulse particle image velocimetry and particle tracking. *Experiments in Fluids*, 56(1):1–12, 2015.

[32] Ansgar Marwege, Sebastian Willems, Ali Gülhan, Michael J Aftosmis, and Eric C Stern. Superposition method for force estimations on bodies in supersonic and hypersonic flows. *Journal of Spacecraft and Rockets*, 55(5):1166–1180, 2018.

[33] Martin R Maxey and James J Riley. Equation of motion for a small rigid sphere in a nonuniform flow. *The Physics of*

Fluids, 26(4):883–889, 1983.

[34] M Mehrabadi, S Tenneti, R Garg, and S Subramaniam. Pseudo-turbulent gas-phase velocity fluctuations in homogeneous gas–solid flow: fixed particle assemblies and freely evolving suspensions. *Journal of Fluid Mechanics*, 770:210–246, 2015.

[35] Y Mehta, Ryan J Goetsch, Oleg V Vasilyev, and Jonathan David Regele. A particle resolved simulation approach for studying shock interactions with moving, colliding solid particles. *Computers & Fluids*, page 105670, 2022.

[36] Y Mehta, TL Jackson, J Zhang, and S Balachandar. Numerical investigation of shock interaction with one-dimensional transverse array of particles in air. *Journal of Applied Physics*, 119(10):104901, 2016.

[37] Y Mehta, C Neal, TL Jackson, S Balachandar, and S Thakur. Shock interaction with three-dimensional face centered cubic array of particles. *Physical Review Fluids*, 1(5):054202, 2016.

[38] Y Mehta, C Neal, K Salari, TL Jackson, S Balachandar, and S Thakur. Propagation of a strong shock over a random bed of spherical particles. *Journal of Fluid Mechanics*, 839:157–197, 2018.

[39] WC Moore, S Balachandar, and Georges Akiki. A hybrid point-particle force model that combines physical and data-driven approaches. *Journal of Computational Physics*, 385:187–208, 2019.

[40] Philip McCord Morse, Acoustical Society of America, and American Institute of Physics. *Vibration and sound*, volume 2. McGraw-Hill New York, 1948.

[41] Andreas Nygård Osnes, Magnus Vartdal, Marianne Gjestvold Omang, and Bjørn Anders Pettersson Reif. Computational analysis of shock-induced flow through stationary particle clouds. *International Journal of Multiphase Flow*, 114:268–286, 2019.

[42] Andreas Nygård Osnes, Magnus Vartdal, Marianne Gjestvold Omang, and Bjørn Anders Pettersson Reif. Particle-resolved simulations of shock-induced flow through particle clouds at different reynolds numbers. *Physical Review Fluids*, 5(1):014305, 2020.

[43] Seong-Hyeon Park and Gisu Park. Separation process of multi-spheres in hypersonic flow. *Advances in Space Research*, 65(1):392–406, 2020.

[44] M Parmar, A Haselbacher, and S Balachandar. Equation of motion for a sphere in non-uniform compressible flows. *Journal of Fluid Mechanics*, 699:352–375, 2012.

[45] C Peng, B Kong, J Zhou, B Sun, A Passalacqua, S Subramaniam, and RO Fox. Implementation of pseudo-turbulence closures in an eulerian–eulerian two-fluid model for non-isothermal gas–solid flow. *Chemical Engineering Science*, 207:663–671, 2019.

[46] JD Regele, J Rabinovitch, T Colonius, and G Blanquart. Unsteady effects in dense, high speed, particle laden flows. *International Journal of Multiphase Flow*, 61:1–13, 2014.

[47] PJ Register, MJ Aftosmis, EC Stern, JM Brock, PM Seltner, Sebastian Willems, Ali Gülhan, and DL Mathias. Interactions between asteroid fragments during atmospheric entry. *Icarus*, 337:113468, 2020.

[48] Arman Seyed-Ahmadi and Anthony Wachs. Microstructure-informed probability-driven point-particle model for hydrodynamic forces and torques in particle-laden flows. *Journal of Fluid Mechanics*, 900, 2020.

[49] Arman Seyed-Ahmadi and Anthony Wachs. Physics-inspired architecture for neural network modeling of forces and torques in particle-laden flows. *Computers & Fluids*, 238:105379, 2022.

[50] Jonathan Richard Shewchuk. Triangle: Engineering a 2D Quality Mesh Generator and Delaunay Triangulator. In Ming C. Lin and Dinesh Manocha, editors, *Applied Computational Geometry: Towards Geometric Engineering*, volume 1148 of *Lecture Notes in Computer Science*, pages 203–222. Springer-Verlag, May 1996. From the First ACM Workshop on Applied Computational Geometry.

[51] Elizabeth A Silber, Mark Boslough, Wayne K Hocking, Maria Gritsevich, and Rodney W Whitaker. Physics of meteor generated shock waves in the earth's atmosphere–a review. *Advances in Space Research*, 62(3):489–532, 2018.

[52] Shankar Subramaniam. Lagrangian–eulerian methods for multiphase flows. *Progress in Energy and Combustion Science*, 39(2-3):215–245, 2013.

[53] Shankar Subramaniam. Multiphase flows: Rich physics, challenging theory, and big simulations. *Physical Review Fluids*, 5(11):110520, 2020.

[54] Shankar Subramaniam and S Balachandar. Towards combined deterministic and statistical approaches to modeling dispersed multiphase flows. In *Droplets and Sprays*, pages 7–42. Springer, 2018.

[55] Bo Sun, Sudheer Tenneti, Shankar Subramaniam, and Donald L Koch. Pseudo-turbulent heat flux and average gas–phase conduction during gas–solid heat transfer: flow past random fixed particle assemblies. *Journal of Fluid Mechanics*, 798:299–349, 2016.

[56] Thomas J Whalen and Stuart J Laurence. Experiments on the separation of sphere clusters in hypersonic flow. *Experiments in Fluids*, 62(4):1–19, 2021.

[57] Wei Xiao, Chaoli Mao, Tai Jin, Kun Luo, and Jianren Fan. Fully resolved simulation of a shockwave interacting with randomly clustered particles via a ghost-cell immersed boundary method. *Physics of Fluids*, 32(6):066105, 2020.

[58] David Zwick and S Balachandar. A scalable euler–lagrange approach for multiphase flow simulation on spectral elements. *The International Journal of High Performance Computing Applications*, 34(3):316–339, 2020.